Geochemistry, Geophysics, Geosystems

RESEARCH ARTICLE
10.1029/2020GC009062

Seismological and Geophysical Signatures of the Deep Crustal Magma Systems of the Cenozoic Volcanic Fields Beneath the Eifel, Germany

Torsten Dahm[1,2], Manfred Stiller[1], James Mechie[1], Sebastian Heimann[1], Martin Hensch[3], Heiko Woith[1], Bernd Schmidt[4], Gerald Gabriel[5,6], and Michael Weber[1,2]

[1]GFZ German Research Centre for Geosciences, Potsdam, Germany, [2]Institute of Geosciences, University of Potsdam, Germany, [3]Geological Survey of Baden-Württemberg, State Seismological Service, Freiburg, Germany, [4]Geological Survey of Rhineland-Palatinate, State Seismological Service, Mainz, Germany, [5]Leibniz Institute for Applied Geophysics, Hannover, Germany, [6]Institute of Geology, Leibniz University Hannover, Germany

Key Points:
- Melts below volcanic fields are narrow zones in the lower crust and upper mantle, identified by low velocities and transparent lower crust
- Deep low-frequency earthquakes can originate from zones of high melt concentration in the upper mantle
- The location of Tertiary and Quaternary volcanic fields can be controlled by preexisting lithospheric structures and terrane boundaries

Supporting Information:
- Supporting Information S1

Correspondence to:
T. Dahm,
torsten.dahm@gfz-potsdam.de

Citation:
Dahm, T., Stiller, M., Mechie, J., Heimann, S., Hensch, M., Woith, H., et al. (2020). Seismological and geophysical signatures of the deep crustal magma systems of the Cenozoic volcanic fields beneath the Eifel, Germany. *Geochemistry, Geophysics, Geosystems*, *21*, e2020GC009062. https://doi.org/10.1029/2020GC009062

Received 27 MAR 2020
Accepted 25 JUL 2020
Accepted article online 30 JUL 2020

©2020. The Authors.
This is an open access article under the terms of the Creative Commons Attribution License, which permits use, distribution and reproduction in any medium, provided the original work is properly cited.

Abstract The Quaternary volcanic fields of the Eifel (Rhineland-Palatinate, Germany) had their last eruptions less than 13,000 years ago. Recently, deep low-frequency (DLF) earthquakes were detected beneath one of the volcanic fields showing evidence of ongoing magmatic activity in the lower crust and upper mantle. In this work, seismic wide- and steep-angle experiments from 1978/1979 and 1987/1988 are compiled, partially reprocessed and interpreted, together with other data to better determine the location, size, shape, and state of magmatic reservoirs in the Eifel region near the crust-mantle boundary. We discuss seismic evidence for a low-velocity gradient layer from 30–36 km depth, which has developed over a large region under all Quaternary volcanic fields of the Rhenish Massif and can be explained by the presence of partial melts. We show that the DLF earthquakes connect the postulated upper mantle reservoir with the upper crust at a depth of about 8 km, directly below one of the youngest phonolitic volcanic centers in the Eifel, where CO_2 originating from the mantle is massively outgassing. A bright spot in the West Eifel between 6 and 10 km depth represents a Tertiary magma reservoir and is seen as a model for a differentiated reservoir beneath the young phonolitic center today. We find that the distribution of volcanic fields is controlled by the Variscan lithospheric structures and terrane boundaries as a whole, which is reflected by an offset of the Moho depth, a wedge-shaped transparent zone in the lower crust and the system of thrusts over about 120 km length.

Plain Language Summary In the mountains of the Eifel in West Germany there are many hundreds of maars and cinder cones, as well as three larger, explosive volcanic centers. The most recent volcanic eruption in the Eifel was only 10,900 BP. Although it is certain that active magma reservoirs among the volcanoes exist, these have not been geophysically mapped to date. We find evidence of active magma reservoirs in the data of existing seismic experiments over these volcanic fields. Thus, an unusual low velocity layer below 30 km depth extends over all young volcanic fields of the region. Our reanalysis of the reflection seismics in the West Eifel confirms a transparent zone in the lower crust above the low velocity layer, which is interpreted as a possible hot zone. At the top of the transparent zone a bright spot is seen in seismic images, which is interpreted as a cooled magma chamber. We suspect that the same type of reservoir is now being refilled in the Eastern Eifel, where deep low-frequency earthquakes align on a channel-like structure connecting the mantle reservoir with the upper crust to about 8 km below the most dangerous volcano of the East Eifel.

1. Introduction

Quaternary volcanism in the western part of Germany is limited to the Eifel region in the Rhenish Massif (RHM). The RHM shield plateau is part of the Rheno-Hercynian fold and thrust belt on the northern flank of the Middle European Variscan belt (Figure 1), an active/passive margin accretion of several microcontinents 300–330 Ma ago. According to Franke (2014) the Variscan belt never reached elevations of 5,000 m and the RHM only built low orogenic topography. However, a renewed uplift of the RHM coincides with the Alpine push, the formation of the Rhine graben starting about 40 Ma ago and the occurrence of massive Tertiary volcanism since 30 Ma. Since then, the crustal stress field in the RHM systematically rotated from an

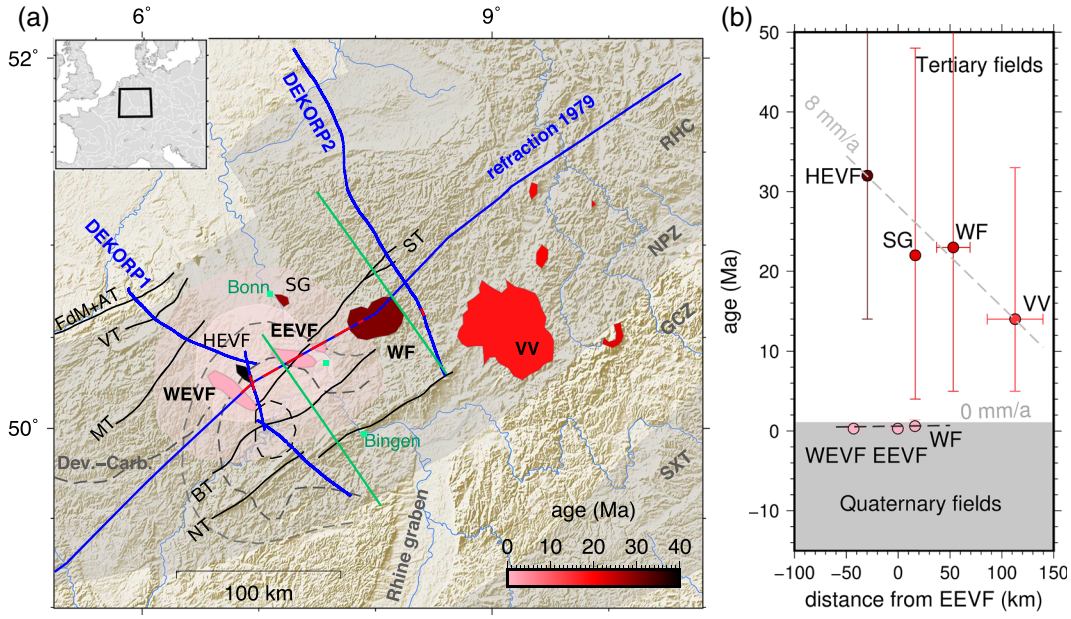

Figure 1. (a) Middle European Variscan belt in the Rhenish Massif with volcanic field regions (filled polygons) colored according to the average age of activity (EEVZ = East Eifel Volcanic Field; WEVF = West Eifel Volcanic Field; HEVF = High Eifel Volcanic Field; SG = Siebengebirge,; WF = Westerwald Field; VV = Vogelsberg volcano). Seismic profiles are plotted as blue lines, with dashed red lines indicating the segments where zones of partial melts at Moho level or Moho steps have been suggested. Major Rheno-Hercynian thrust and crustal scale ductile shear zones are labeled (NT = Nahe Thrust; BT = Boppard Thrust; ST = Siegen Main Thrust; Dev.-Carb. (dashed) = Devonian-Carboniferous boundary; MT = Malsbender Thrust (dipping to north); VT = Venn Thrust; FdM + AT = Faille du Midi and Aachener Thrust). The areas of accreted microcontinents (SXT = Saxo-Thuringia; GCZ = Middle German Crystalline Zone; RHC = Rheno-Hercynian; NPZ = Northern Pyllite Zone) are indicated by shaded arcs/belts. Dashed closed polygons indicate Moho upwelling (28 to 30 km) as derived from receiver functions (Budweg et al., 2006). Overlaid, transparent, reddish regions indicate the reduced *S* wave mantle velocities (1.4% and 2.8%) between 50 and 100 km depth (Keyser et al., 2002). (b) Age of the larger Quaternary and Tertiary volcanic rocks projected on the refraction profile of 1979. Bars cover the spatial distribution and temporal periods of activity. Migration velocity (average) is indicated by dashed line.

extensional stress regime with a maximum horizontal compression at $\sigma_H \approx$ N20°E via a σ_H in N-S direction during the Tertiary to $\sigma_H \approx$ N307°E and a strike-slip regime today (Hinzen, 2003). Uplift in the RHM accelerated during the Miocene about 15 Ma years ago and continues until today (e.g., Fuchs et al., 1983; Kreemer et al., 2020). However, no single block uplift can be observed in the RHM, but rather a time-changing, small-scale pattern of uplifts, stagnations or depressions, that correlate with volcanic activity.

The first volcanic activity in the Eifel, the so-called Hocheifel volcanic field (HEVF), developed in the Tertiary 39–44 and 35–37 Ma ago (Fekiacova et al., 2007; Lippolt, 1983) during the initial period of the formation of the Cenozoic graben systems. It is characterized by basanitic scoria cones, maars, and a few phonolitic centers (Mertes, 1983). Further east in the RHM the Westerwald volcanic field (WF, ≈800 km^2, Figure 1) developed maars and scoria cones between 20 and 30 Ma and at 5.5 Ma (Haase et al., 2004). However, the largest volumes of Tertiary magmas have been erupted 9–19 Ma ago at the only strato-volcano in the RHM, the Vogelsberg volcano (VV, Figure 1). The VV erupted first phonolitic and later more alkali-basaltic and tholeiitic mafic rocks (Bogaard & Wörner, 2003; Lippolt, 1983). Other smaller Tertiary volcanic fields in the RHM (Northern Hessian, Rhoen) have a similar age as the VV, with the exception of the Siebengebirge volcanics close to Bonn, which are slightly older (Figure 1).

In the Quaternary, since about 0.7 Ma, two spatially separated volcanic fields have formed east and west of the HEVF (Figure 1, Förster et al., 2020; Schmincke, 2007). The so-called West Eifel Volcanic Field (WEVF) comprises about 240 basanitic (mafic) scoria cones and maars (Figure 2a; Mertes, 1983), with the youngest eruption at the Ulmener Maar (UM in Figure 2) 10,900 BP (Zolitschka et al., 1995). The East Eifel Volcanic Field (EEVF) about 60 km east of the WEVF comprises about 100 scoria cones, several maars, and

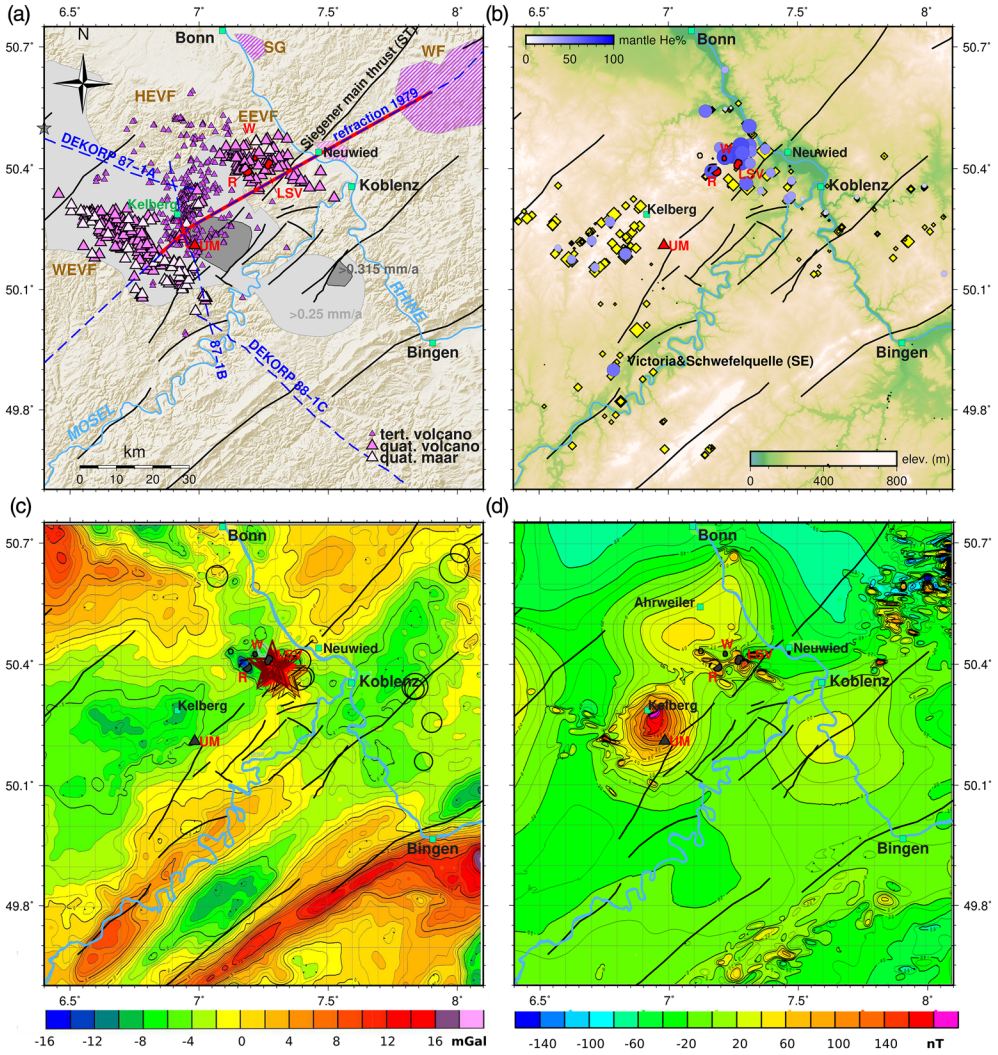

Figure 2. Various geophysical field data are compared in the region of the Eifel volcanic fields (triangles) and Variscan faults (black lines). SG and HEVF indicate the Tertiary volcanoes of Siebengebirge and the high Eifel, respectively. The phonolitic eruption centers of the EEVF, Rieden (R), Wehr (W), and Laacher See volcano (LSV), are indicated by labeled red polygons. The youngest maar in the WEVF, Ulmen (UM), is indicated by the red triangle. Cities are labeled by green squares. (a) Volcanic fields in the RHM plotted together with zones of maximum Quaternary uplift (dark gray>0.3125 mm/year, light gray >0.25 mm/year; from Meyer & Stets, 2007). The maximal instantaneous uplift (Kreemer et al., 2020, ≈1 mm/a) is indicated by the gray star at 6.4°E, 50.5°N. The refraction seismic profile from 1979 and the steep-angle reflection profiles (DEKORP) are plotted as blue, dashed lines. Red underlined sections are described in Figure 1. (b) Mofettes and CO_2-rich springs/wells in the RHM. The blue circles indicate the mantle contribution based on helium isotopes (mantle He% = Ra/8, see color scale - size scales to mantle He%; from Bräuer et al., 2013; Griesshaber et al., 1992). CO_2-rich springs/wells are plotted as yellow diamonds, scaled by flow rate - maximum at 6,000 mg/L. The Victoriaquelle and Schwefelquelle (SE) are labeled, the topography is plotted in the background. (c) Bouguer anomaly. A linear regional trend has been removed (−15.26 mGal/km in NE-E direction). Filled stars depict the DLF earthquakes between 2013 and 2019 (see Figure 3 for color scaling). Open gray circles show tectonic earthquakes between 1975 and 2014 with ML > 3, with the largest earthquake at $M_L = 5$. (d) Magnetic total field anomalies (DGRF 1980, LIAG).

additionally three phonolitic eruption centers at Rieden (≈450 ka), Wehr (≈150 ka), and the Laacher See volcano (LSV), respectively (Figure 2a). The LSV had its first and so-far only Plinian VEI 6 eruption in 12,880 ± 40 BP (Brauer et al., 1999).

The Quaternary WEVF and EEVF occur above a 100 km broad seismic *S* wave anomaly in the upper mantle and a broader region of Moho upwelling as documented by receiver functions (Figure 1). Therefore, a plume-like upwelling of asthenospheric and lithospheric mantle rocks has been suggested

(Ritter et al., 2001), which may possibly have even deeper roots in a lower mantle plume with a stem radius of 60 km and a center about 50 km to the S of the WEVF and 80 km S-SW of the EEVF (Ritter, 2007; Wüllner et al., 2006).

The Quaternary and Tertiary volcanic fields in the RHM occur within an EW trending belt (Figure 1a) as could be expected for a typical hot spot track. However, the temporal pattern of volcanic activity cannot be explained by the unidirectional motion of a deep mantle plume (Figure 1b). Apart from this, the mantle plume hypothesis for the Eifel has other issues, which render it at least uncommon. For instance, the volume of magma expelled at the surface is small compared to established intraplate hot-spot volcanoes as in Iceland or Hawaii. Haase et al. (2004) showed that the source of basanitic lavas at the VV was shallow and possibly related to a thermal boundary layer at the base of the lithosphere, instead of a homogeneous mantle upwelling as suggested for the EEVF and WEVF (and WF). Additionally, the distribution of volcanoes within single fields follows a NW-SE trend (Figure 2a), which is different to the W-SW motion of the assumed deep mantle plume predicted from plate tectonic models and indicated from the asthenospheric *S* wave velocity anisotropy beneath the Eifel (Walker et al., 2007).

Other models explain the anorogenic Tertiary to present uplift and volcanism of the RHM by the lithospheric response (mantle upwelling) to an asthenospheric thermal instability (e.g., Garcia-Castellanos et al., 2000, see also Pfaender et al., 2018), or the regional-scale reorganization of mantle flow after the Alpine collision (Wilson & Downes, 2006; compare also to the model by Yang & Faccenda, 2020). This view is supported by mantle xenoliths from Tertiary volcanics, equilibrated at 950–1150°C, which are similar to Quaternary xenoliths of the WEVF indicating static conditions (nontransient) in wide parts underneath the RHM as can be explained by mantle up-doming (Seck & Wedepohl, 1983).

Independent of the existence of a deep lower mantle plume, the magmatism in the RHM is a product of the interaction of upper mantle upwelling, tectonic stressing, and preexisting lithospheric structures and slab suture zones/terrane boundaries developed during the Variscan collision, where several minor continental terranes and basins (Saxo-Thuringian, Mid-German Crystalline Zone, Rheno-Hercynian, Figure 1) were successfully accreted and shortened by 52% (Franke et al., 2017; Koenigshof et al., 2016; Oncken et al., 1999). Their geological records, faults, and folds indicate trends parallel to the distribution of Cenozoic volcanoes (Figure 1). The beginning of accretion during Late Devonian and Early Carboniferous involved the NW-directed subduction of the large Rheic and later the SE subduction of the intervening Rheno-Hercynian oceanic basins. Despite the massive accretion, the continental crust beneath the RHM has nowadays a thickness of only 30 km, maybe because of the relatively high temperature of the Variscan orogen and the possible delamination and disappearance of the lithospheric mantle and lower Rheno-Hercynian crust (Franke et al., 2017; Pfiffner, 2017). This could cause the upper mantle under the RHM to be thermally unstable and conditioned for the formation of partial melts.

The volcanism in the RHM was and is fed from lower crustal and upper mantle melt reservoirs. Understanding the geometry, structure, and state of such deep reservoirs is a key to understand most of the volcanism in the Eifel and anorogenic distributed, continental volcanic fields in general. Models of hot, high-melt-fraction "magma-chambers" have dominated the schools of crustal magmatism over decades (e.g., Marsh, 1989). However, recent investigations increasingly point to the existence of cold, low-melt-fraction reservoirs in the lower crust and upper mantle, so-called mush reservoirs (e.g., Annen et al., 2006). In the mush concept, a reservoir first develops in the upper mantle and lower crust by repeated intrusions of dikes and sills over longer periods, possibly along preexisting structures of weakness. As long as the repose period of sill intrusions is much shorter than the total duration of basalt emplacement, the long-term evolution is controlled by the average emplacement rate (Annen et al., 2006). Assuming average intrusion rates of about 10^{-2} km^3/a, a significant temperature increase of ≈200°C in the lower crust is reached after 10^5 to 10^6 years (e.g., Karakas et al., 2017). Lower-crust intrusion rates beneath the EEVF are estimated in the range of 5×10^{-4} km^3/a, and would therefore need several million years to generate a hot lower-crustal mush reservoir. Mush reservoirs may resolve some of the geochemical and geophysical paradigms of the chamber models for the Eifel, as they (1) can explain the variations in chemical composition of the Eifel melts (e.g., Mertes, 1983; Schmincke, 2007), (2) explain the rapid reactivation and transport of magma to the surface before the last VEI 6 eruption of the LSV (e.g., Rout & Wörner, 2018; Schmitt, 2006), and (3) explain the lack of geophysical evidence of volumetric

high-melt-fraction bodies under the EEVF and WEVF, taking into account the longevity of the LSV reservoirs (Schmitt et al., 2010).

In this study, we compile information on deep earthquakes, the degassing of magmatic fluids, and different geophysical data from the crust in the RHM. We present reprocessed seismic lines and discuss them together with refraction seismic experiments from 1978/1979 and the occurrence of deep low-frequency (DLF) earthquakes and earthquake swarms beneath the EEVF. We discuss this information in the context of mushy melt reservoirs in the upper mantle and lower crust beneath the Eifel and estimate possible melt fractions in low velocity zones.

2. Magmatic Systems beneath the RHM: State of Knowledge

We compile different information and results, which are suitable to narrow down the structures of magmatic reservoirs in the upper mantle and the crust.

2.1. Moho Upwelling, Upper Mantle Velocity Anomalies, and Uplift Regions

A Moho upwelling beneath the WEVF, derived from receiver functions (Budweg et al., 2006), roughly correlates with a negative *S* wave velocity (v_s) anomaly of up to −5% at 30–100 km depth (Keyser et al., 2002) (Figure 1) and reduced upper mantle *P* wave velocities (v_P, Ritter et al., 2001). A classical plume head, leading to a mushroom like velocity anomaly in v_p and v_s, is absent. The v_s anomaly is absent between 170 and 240 km depth and has a large E-W extension below. The anomalous low v_P beneath the West Eifel can be explained by 200°C excess temperatures in the upper mantle up to 1200–1300°C, a few percent of partial melts (Ritter, 2007), and a buoyancy flux of 500–1,000 kg/s (Wüllner et al., 2006). The measured heat flux in the WEVF of 70–80 mW/m^2 is lower than expected from a deep mantle plume assuming steady-state conductive heat transfer, indicating that the thermal perturbation beneath the Eifel is possibly small (Seck & Wedepohl, 1983).

The uplift of the RHM since Quaternary (Westerwald ≈ 250 m, Hohe Venn ≈ 460 m, see Fuchs et al., 1983; WEVF and Ardennes ≈ 250 m, see Meyer & Stets, 2007; Garcia-Castellanos et al., 2000) indicates an uplift rate of up to 0.3 mm/a and includes regions outside the area of the v_s anomaly (Figure 2a). The present-day uplift estimated from the Global Positioning System indicates higher rates of 1 mm/a with a center NW of the WEVF (Kreemer et al., 2020, Figure 2a).

2.2. Geochemical Signatures of the Mantle Source of Volcanics

Partial melts must be present in the upper mantle and lower crust to explain the Quaternary volcanism. Mantle xenolith diffusion studies of high temperature harzburgites (1280°C) from 80 km depth indicate that already during the Cretaceous a rapid mantle heating event occurred within 1 Ma (Witt-Eickschen, 2007). After this, the upper mantle was slowly cooled down over a period of 130 Ma (porphyroclastic xenoliths at 30 km, from 1100 to 800°C). However, locally, a rapid (<0.5 Ma) reheating at a depth of 50 km or shallower is indicated by xenoliths (Witt-Eickschen, 2007). In general, the geochemical signatures of the volcanics, the eruption styles, and vent distribution of the Quaternary and Tertiary volcanic fields in the Eifel and Westerwald are similar. The isotopic and chemical composition of the lavas and mantle xenoliths of the WF (Seck & Wedepohl, 1983) both indicate a mid-ocean ridge basalt (MORB-type) mantle source at about 50 km depth, similar to the ones found for the EEVF and WEVF. Despite this coincidence it is debated whether the HEVF and WF are genetically related to the Quaternary EEVF and WEVF and other volcanic fields (e.g., Fekiacova et al., 2007).

Measured major and trace element concentrations of sampled lava flows in the WEVF together with $^{40}Ar/^{39}Ar$ age data show a spatiotemporal separation of activity in the sense that lava flows with ages >480 ka occurred exclusively NW and <80 ka exclusively SE of the volcanic field (Mertz et al., 2015). While the older activity in the NW showed significant thermal erosion and lithospheric interaction at shallow mantle levels, the parental magmas from the younger activity in the SE come from a depth >70 km. Trieloff and Altherr (2007) confirm the dominant lithospheric geochemical source signature, but see, however, also indications for possible deeper mantle components in their volatile studies.

Table 1
Comparison of the WEVF, South Eifel (SE), and EEVF

		WEVF	SE	EEVF	Reference
Area	km^2	600		400	Schmincke (2007)
erupted material	km^3	1.7		>6.3	
residual magma	km^3			60	
number of volcanoes		240		100	
number of springs with CO_2 > 1 g/l		89	29	85	Landesamt für Geologie und Bergbau, Rheinland Pfalz
CO_2 flux	kt/a	16.4		60–85	May (2002)
$\delta^{13}C_{CO2}$	‰		−2.0[a]	−4.6	Bräuer et al. (2013)
$^3He/^4He$	R_A	2.66[b]	4.3[a]	5.6	
$\delta^{15}N$	‰		−2.5	7	
$^{40}Ar/^{36}Ar$		1060[b]	3670[c]	400	

Note. The $^3He/^4He$ ratio measured in the sample is corrected for atmospheric contamination and R_A is the atmospheric $^3He/^4He$ ratio of 1.38×10^{-6} (Anderson, 1998).
[a]Victoria and Schwefelquelle located S of West Eifel. [b]Wallenborn—Aeschbach-Hertig et al. (1996). [c]Bekaert et al. (2019) report a ratio of 8,287 at Schwefelquelle.

2.3. Fluid Geochemistry and Mantle-Derived CO_2

Both volcanic fields (WEVF and EEVF) are accompanied by hundreds of CO_2-rich springs and mofettes with the highest concentration in the centers of the EEVF and WEVF, and a longer tail of the distribution toward the south and southeast. The occurrence of springs with a free gas phase is partly controlled by tectonic lineaments with a Variscan trend (Figure 2b). The total CO_2 flux is possibly 0.5 to 1 Mt/a (Puchelt, 1983), and is partly utilized for mineral water and/or industrial gas production. In the WEVF the commercial production accounts for nearly 90% of the total C flux of 11,811 mol/s (~16.4 kt/a, May, 2002, and Table 1). In the EEVF the Wehr phonolitic center (W in Figure 2b) is possibly the largest CO_2 reservoir, with a production of up to 9 t/hr (82.1 kt/a) from seven wells by CARBO industries (from https://www.carbo.de/de/ueber-uns in 2019). For comparison, the CO_2 flux from the LSV is estimated at 5 kt/a (Aeschbach-Hertig et al., 1996).

Bräuer et al. (2013) studied the composition and isotope ratios of CO_2 and He of 25 degassing locations in the EEVF and WEVF and two locations further to the south. They found that $\delta^{13}C_{CO2}$ signatures of unfractionated gas at the EEVF are consistent with the MORB range. Carbon isotope values ($\delta^{13}C_{CO2}$ V-PDB) are on average -4.6 ± 0.6‰ and He isotope ratios R_C/R_A are up to 5.6 (Table 1). In the EEVF the $\delta^{13}C_{CO2}$ values and R_C/R_A ratios are highest at the Laacher See and Wehr and decrease north and south of these two phonolitic centers (Figure 2b). The high isotope ratios in the central anomaly show little crustal contamination, indicating that CO_2 beneath the Laacher See migrates quickly from its magma source to the surface. Bräuer et al. (2013) conclude that these gases originate from an active magma source in the mantle.

Differences in isotope signatures in the WEVF and the more southern mofettes indicate that the regions are most likely supplied by magmatic reservoirs with different melt compositions and/or melt fractions. Degassing locations in the WEVF, close to the center of the v_S anomaly, could not confidently be characterized as having a mantle source, as a considerably stronger crustal influence is observed.

Recent high precision analyses of Ne, Ar, and Xe isotopes sampled in springs in the South East Eifel (Victoriaquelle and Schwefelquelle wells, Figure 2b, Table 1) indicate that the mantle beneath the Eifel volcanic area resembles more a convective upper mantle reservoir (MORB-type) than a deep plume source (Bekaert et al., 2019). Ne and Xe systematics point toward contributions from multiple reservoirs with different degassing, supporting the interpretation of Bräuer et al. (2013).

2.4. Gravity Field Anomaly

While individual maar structures give rise to local negative gravity anomalies and models of the size and depth of the maars can be developed (e.g., Sebazungu, 2005), the regional gravity data in the RHM give little evidence of heavy magmatic bodies in the crust and upper mantle leading to positive Bouguer anomalies. Ritter et al. (2007) have calculated forward models of the Bouguer anomaly of the seismic mantle plume and estimated long-wavelength anomalies in the gravity field of −10 mGal. Anomalies of this size are

overprinted in the regional maps by the influences of heterogeneities in the upper crust. Moreover, for magma bodies that reside in the crust at a level of neutral buoyancy, small density contrasts relative to the host rock can be assumed. Although the magnitude of the density contrast also depends on the rheological state of the crust, magma bodies of limited extent cause only small gravity anomalies that are hardly distinguishable from other intracrustal sources. Intracrustal sources of larger extent become visible in the detrended regional gravity map that shows linear anomalies parallel to preexisting structures of the RHM. The Northern Phyllite Zone (NPZ) and the Mosel syncline appear as gravity highs up to +12 mGal elongated over 50 and more kilometers, while the zones northwestward indicate negative Bouguer values of −8 mGal, including the WEVZ and EEVZ (Figure 2c). The local Bouguer low at Rieden is −13 mGal (Figure 2c). As will be discussed below, the zones of positive Bouguer values do not correlate with sections of thinner crust at the volcanic fields. This indicates a local compensation of the crustal thickness effect by density variations in the lower crust or upper mantle.

2.5. Magnetic Field Anomaly

The WEVF, EEVF, and WF are recognized in the magnetic maps as regions with strong fluctuations of the total magnetic field (Figure 2d, see Gabriel et al., 2011), since the multiple superficial intrusions and volcanic tephra create a pattern of short-wavelength dipole anomalies. South of the Mosel river in the Saar-Nahe basin (SW of Bingen in Figure 2d) short-wavelength, dipole-like anomalies are caused by older superficial intrusions from the Permo-Carboniferous volcanism between 289 and 292 Ma (Lippolt & Hess, 1989). At the eastern border of the WEVF, close to Kelberg, a larger circular magnetic anomaly with a diameter of about 30 km and a maximum of 182 nT is prominent, the so-called "Kelberg magnetic high" (Figure 2d, see also Büchel, 1990). Pucher (1992) modeled the anomaly by magnetized, Tertiary sill-like intrusions of several kilometers lateral extent in 8–13 and 3–7 km depth, with a magnetization of 0.76 and 0.67 Am^{-1} and a declination and inclination of D ≈ 0° and I ≈ 68°, respectively. Alternatively, Pucher (1992) explains the Kelberg high by assuming a magnetization (0.9 Am^{-1}) between 8 and 12 km depth of a thermal contact aureole in the Devonian rocks above a hot (mushy, light) reservoir in the middle to lower crust (described as a pluton). The magnetic anomaly results from a superposition of remanently magnetized basement rocks in the Paleozoic direction (D ≈ 220°, I ≈ 5°) superposed by an induced magnetization with D ≈ 0° and I ≈ 67°. As the field direction of the Tertiary is similar to the current magnetic field, the modeling cannot distinguish between a cooled Tertiary and Quaternary magma reservoir.

In the EEVF, a strong long-wavelength magnetic anomaly is visible near Ahrweiler at the NW border of the three phonolitic centers Rieden, Wehr, and LSV (Figure 2d). The anomalies at the volcanic centers themselves are of shorter wavelength and complex shape and are explained by magnetized tephra layers from previous eruptions. Pucher (1992) also investigated the Quaternary EEVF magnetic anomalies and estimated the strength and direction of magnetization from basaltic samples with an age of ≈0.5 Ma. The Curie temperature was measured between 460 and 550°C. Interestingly, in contrast to Kelberg, after removal of the magnetic anomalies by near-surface source bodies below the phonolitic centers, there is no magnetic evidence of an upper crustal, solidified magma body as predicted by geochemistry. For example, geochemical model calculations indicate that the LSV eruption of 12.9 ka ago alone created a residual magma reservoir of about 60 km^3 in the crust, with 11 km^3 at shallow levels above 6 km depth (Wörner & Schmincke, 1984). The absence of a strongly magnetized body below the LSV led Pucher (1992) to assume that the residual magma reservoir of the last LSV VEI 6 eruption is still too hot to cause significant remanent magnetization.

2.6. DLF Earthquakes

DLF microearthquakes observed in some volcanic areas are commonly interpreted as signs of magmatic unrest and magmatic fluid migration (e.g., Kurihara et al., 2019). DLF earthquakes contain frequencies well below the typical corner frequency of tectonic microearthquakes, and show additionally long coda waves with dominant frequencies in the range between 1 and 10 Hz. Since the improvement of the permanent seismic network in Rhineland-Palatinate, persistent bursts of DLF earthquakes with magnitudes M < 2 have been detected beneath the LSV, first observed in 2013 (Hensch et al., 2019). The DLFs occur in short bursts and align on a channel-like structure from 43 km to about 8 km depth (Figure 2c). This indicates that mantle-CO_2 or other magmatic fluid migrates along this channel from the upper mantle to the LSV. Hensch et al. (2019) suggest that the location of DLF clusters below the LSV indicates the positions of

magmatic reservoirs in the upper mantle and crust that experience a sudden increase in pressure. As the DLF bursts occur regularly at persistent depth ranges, it is possible that the upper and midcrustal magmatic reservoirs beneath the LSV are currently being recharged by the influx of magmatic fluids or magmas from below. However, magmatic reservoirs have not yet been imaged by independent geophysical studies. Alternative models for DLF earthquakes, not applicable to the LSV, suggest filtering of higher frequencies due to hot material or fluids between source and receiver at Askja volcano in Iceland (Soosalu et al., 2010), the dehydration of serpentinized peridotite due to localized heating in the forearc of the subduction zone of the northern U.S. west coast (Vidale et al., 2014), or to be caused by a "secondary boiling" in stalled deep intrusions beneath Mauna Kea (Wech et al., 2020).

3. Seismic Profiling of Magmatic Systems

3.1. Wide-Angle Refraction Lines

A 600 km long seismic profile ranging from the Paris Basin in the southwest, across the RHM, to the Hessian Depression in the northeast was conducted in 1979 (Mechie et al., 1982, 1983, Figure 1). Explosive shots were fired roughly every 75 km at nine locations along the profile (A to I in Figure 3). A cross profile of 170 km length was fired directly over the WEVF in 1978, and data from previous experiments in the eastern RHM from 1958 and 1974 were included in the analysis. The average spacing of three component geophones (1 and 2 Hz seismometers) along the main and cross profiles was 2 and 3 km, respectively, leading to about 3,000 seismogram recordings. Signal-to-noise ratio of band-pass filtered seismograms (1.3–33 Hz) was sufficient for the correlation of body wave phases up to 250 km distance from the shot-points. The analysis comprised a preliminary 1-D inversion of velocity depth functions coupled with a 2-D trial-and-error forward modeling using ray tracing and was combined with amplitude interpretation by comparison with full synthetic reflectivity seismograms (see Mechie et al., 1983).

First arrival refracted and second arrival reflected *P* waves were correlated, picked, and interpreted in terms of different sedimentary, intracrustal, and upper mantle layers. The 2-D ray-tracing model of Mechie et al. (1983) is presented here (Figure 3). Reciprocity of the theoretical travel times is automatically guaranteed by the 2-D ray-tracing procedure. For shot-points D and F, which are about 90 km apart, the phases PmP^1 and PmP^2 can both be recognized in the observed data close to the theoretical travel-time curves. PmP^1 is the reflection from the top of the high velocity layer at ca. 29 km depth. PmP^2 is the retrograde phase from close to the base of the transition zone at ca. 35–36 km depth (see also supporting information Figure SB1). The fit between the theoretical and observed travel times is good for all phases. For phase PmP^1 the average absolute time difference between theoretical and observed arrivals is 0.12 s (130 observations). For PmP^2 it is 0.06 s (24 observations). For all the phases it is 0.08 s (517 observations)—see also Mechie et al. (1983). The thickness of low velocity layers was mainly constrained by fitting the critical point of the reflected phase from the high-velocity layer immediately below (Figure SB1). In some cases a thin high-velocity layer above a low-velocity layer was identified (e.g., at the crust-mantle boundary at 29 km depth at distance 0 km in Figure 3) by the absence of a refracted wave propagating in the thin high-velocity layer on top (compare to Figure SB3). The analysis of amplitude ratios for phases from the crust-mantle transition region constrains an approximately 6 km thick transition zone below the thin high-velocity layer at 29 km depth. This low-velocity layer correlates with the EEVF at its center and with the depth and location of DLF earthquakes beneath the LSV (Figure 3). As the velocities jump at a depth of 29 km to mantle velocities, and because a few kilometers north and south of the profile the Moho lies at about the same depth, Mechie et al. (1982, 1983) placed the low velocity layer in the upper mantle. In summary, a 6 km thick low-velocity transition zone was identified below 30 km depth in the upper mantle directly below the Moho and beneath the volcanic fields, which extends along the trend of Variscan structures from the WEVF via the EEVF to the WF. Although Mechie et al. (1982, 1983) indicate that partial melts may explain such low-velocity layers, the finding was not interpreted as a case of active magmatic reservoirs beneath the Quaternary volcanic fields. Interestingly, from the WEVF to the WF, the lower crust also shows a pronounced low-velocity zone upwelling in the center of the segment (Figure 3), although the relative velocity decrease is smaller than in the upper mantle.

Possible upper mantle reflections (retrograde phases) were also recorded both to the southwest and northeast of shot-point D at distances between 200 and 250 km (Mechie et al., 1982, 1983, and Figure SB1).

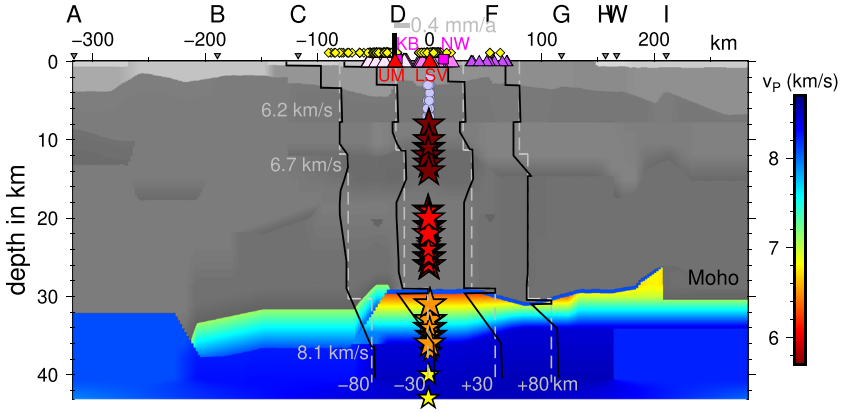

Figure 3. *P* wave velocity model of the crust (gray scale) and upper mantle (colored scale) along the refraction seismic profile from 1979 (from Mechie et al., 1983, see Figure 2 for location). The positions of DLF earthquakes between 2013 and 2019 are plotted as colored stars, where symbol size indicates the magnitudes of events ($0.7 < Mw < 2.7$). The shallow earthquakes from the Glees swarm occurring after the largest DLF burst in 2017 are plotted as blue circles. The position of the intersecting profile DEKORP 1B is indicated as a vertical bar. Locations of Quaternary scoria cones and maars and Tertiary volcanoes are plotted as triangles. The LSV (EEVF) and Ulmener maar (UM, WEVF) are highlighted by red triangles. The Westerwald field is at shot point F. The projected locations of the cities Neuwied and Kelberg are denoted by squares. *P* wave velocity-depth functions are plotted as black lines for ±80 and ±30 km. The dashed, gray velocities indicate reference velocities of 6.2, 6.7, and 8.1 km/s for the upper and lower crust and the upper mantle, respectively. A–I indicate the positions of explosive sources.

Mechie et al. (1982) interpreted these phases as being produced by transition zones in the upper mantle with a velocity increase with depth. According to Mechie et al. (1982) the bottoms of these transition zones occur at 47–49 km depth and they are located 105–115 km SW and 110–125 km NE of shot-point D (Figure 3). However, the position of the reflectors in the upper mantle may shift if the reflectors were tilted. The strong gradient zones could just as well be first-order discontinuities and instead of a velocity increase with depth a velocity decrease with depth could also be possible. If a velocity decrease with depth would occur, this could be due to either some amount of partial melt in the rocks or anisotropy.

3.2. Steep Angle Reflection Experiments

The German Continental Seismic Reflection Program DEKORP (DEutsches KOntinentales Reflexionsseismisches Programm) was carried out between 1984 and 1999 as the German national reflection seismic program funded by the Federal Ministry of Research and Technology. The aim of DEKORP in the western part of the RHM was to investigate the deep crustal structure of the Eifel with high-fold, high-resolution near-vertical incidence vibro-seismic acquisition (for field parameters see Table SC1), supplemented by wide-angle seismic and other target-oriented piggy-back experiments, all complemented by optimized methods of data processing and interpretation. The DEKORP-Atlas (Meissner & Bortfeld, 1990) gives a detailed overview of most of the different campaigns and results. The profiles 1A, 1B, and 1C (Figures 1 and 2a) were recorded in 1987 and 1988 as part of DEKORP.

The 93 km long, WNW-ESE trending DEKORP 1A line crosses the Variscan foreland in Belgium, the northern Variscan Deformation Front (AT in Figure 1), and the Stavelot-Venn Anticline (VT), arcing around a north-south trending depression zone (so-called Eifel N-S-zone). The nearly N-S trending DEKORP 1B line has a length of 50 km and intersects DEKORP 1A near the town Adenau. It crosses the WEVF, the Kelberg magnetic high, and the Siegen Main Thrust and ends in the Mosel Syncline (Figure 2a). Merging with line 1B, line 1C starts in the Mosel syncline and trends WNW-ESE into the Permian Saar-Nahe basin. Its total length is 75 km. The angle of crossing is ca. 152°. The seismic profile crosses the Devonian Hunsrück slate belt with the Hunsrück boundary fault and NPZ, separating the Rheno-Hercynian and Mid-German Crystalline Zone, respectively, the Saxo-Thuringian (Figure 1).

The initial processing in the 1980s was conventional (normal moveout correction + post-stack migration only, see Meissner & Bortfeld, 1990). Results of the DEKORP 1 campaigns are found in DEKORP Research Group (1991). In the years 2018–2020, several DEKORP lines were reprocessed with state-of-the-

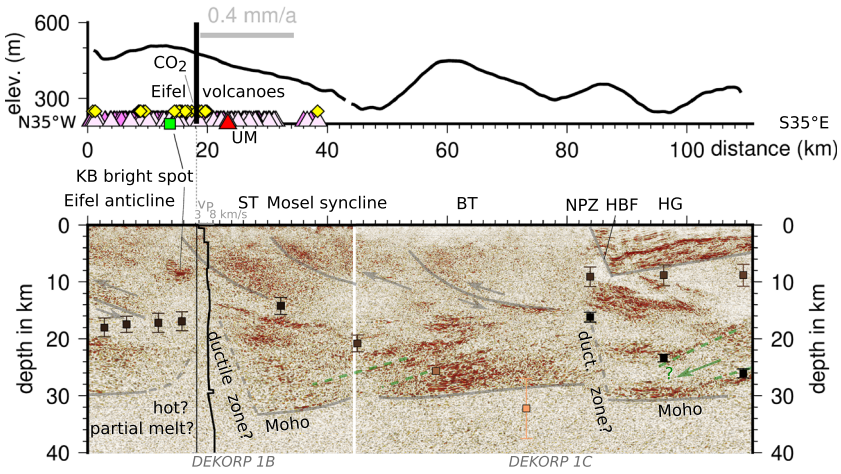

Figure 4. Prestack, depth-migrated section of DEKORP 1B and DEKORP 1C, concatenated at the crossing point and projected on to a single profile with an average azimuth. Kilometer scale indicates projected length. Abbreviations: ST, BT, HBF = Siegen Main Thrust, Boppard Thrust, Hunsrück Boundary Fault; NPZ = Northern Phyllite zone; HG = Saar-Nahe Half-Graben. The Mosel syncline and Eifel anticline are indicated. The Kelberg (KB) bright spot is indicated. The *P* wave velocity-depth function (v_P) from the crossing refraction seismic line is plotted as black line. Colored squares show projected positions of high conductivity layers/zones after Jödicke 1983 (black = 2 Ωm, light red ≈40 Ωm, see Figure 1 for MT profiles). Tectonic-structural features are indicated by gray and green lines. The upper diagram shows the topography along the profile, the region of maximum Quaternary uplift (gray bar), and the projected volcanoes from EEVF, WEVF, and WF (see Figure 2 for definition of symbols). Yellow diamonds give projected locations of mineral springs from the WEVF (±10 km) with a free gas phase. The position of the intersecting seismic refraction profile (refraction 1979) is indicated as a vertical bar.

art processing methods (common reflection surface (CRS) moveout corrections + prestack depth-migration, see Table SC2 and Stiller et al., 2020a, 2020b, 2020c). Seismic processing was carried out in different steps, starting with CRS stacking and poststack time-migration, followed after successively improved velocity model building by prestack time-migration and finally prestack depth-migration of CRS processed common image gathers. With this, the seismic images could be significantly improved and interpretation becomes more reliable.

Figures 4 and SC1 show the results of the prestack depth-migrations for profiles DEKORP 1B and 1C, newly processed in 2020. The two profiles are concatenated at their crossing points and comprise a total projected horizontal length of about 111 km on a profile from the northern end of 1B to the southern end of 1C. The depth-migrated section is shown with the vertical axis extending to a depth of 40 km.

In the upper and middle crust, south of the NPZ, sedimentary reflections are clearly visible in the Saar-Nahe Half-Graben (HG) to a maximum depth of 9 km. The HG, the largest Permo-Carboniferous basin in the inner zone of the Variscides, is bounded to the north by the Hunsrück boundary fault. It formed during oblique extension (>35%) along an inverted Variscan thrust (e.g., Henk, 1993; Korsch & Schäfer, 1995). The NPZ is the result of multiple folding of an imbricate belt of partially mylonitic rocks, which has functioned as a ductile shear zone (Oncken et al., 1999). The suture zones from the northward subduction of the Rheic ocean and the passive margin of the Rheno-Hercynian ocean are both at the NPZ (Franke et al., 2017). These suture zones have been reactivated during the Tertiary, first by convergence along the NE-SW trending boundary faults, and after the rotation of the stress field during the formation of the Rhine graben system by additional dextral strike-slip movement. The highly reflective filling of the HG is associated with Permo-Carboniferous sediments sitting on a nonreflective, transparent zone, which is associated with the Mid-German Crystalline Zone and represents the (accreted) crystalline basement of the Saxo-Thuringian. The reflecting zone below is according to Henk (1993), a part of the remaining, oceanic crust of the Rheic, which subducted about 400 Ma ago at the NPZ beneath the Rheno-Hercynian crust. Alternatively, it may represent a residual part of the continental lower crust of the Saxo-Thuringian.

The depth of the Hunsrück boundary fault has been controversially discussed. While Meissner et al. (1980) suggest a deeply penetrating, south-westward dipping boundary fault leading to a Moho offset, Henk (1993)

suggests a listric boundary fault of the HG to a depth of about 16 km and does not confirm a Moho offset beneath. Our reprocessed prestack depth-migration of DEKORP 1C confirms the Moho offset, but does not indicate the offset to be related to the south-westward dipping boundary fault, but more likely indicates a residual part of subducting lower crust toward the north-east.

In the lower crust, energetic reflective bands are clearly visible. The sudden decrease in reflectivity at the lower end of the lower crustal reflective bands is interpreted as Moho and thus follows common practice in the interpretation of crustal surveys. The reflective bands in the lower crust become thinner from north to south (see Figure SC2). Correspondingly, the upper crust becomes thicker from north to south. In the middle crust, reflective bands are not as distinct and are more frequently interrupted. In at least two zones along the profile, from 15 to 26 km and from 82 to 88 km horizontal distance, the reflecting band disappears in the lower crust. The lower crust appears transparent at these locations, as significant scattering energy is missing. Either the transparent zones lack any impedance contrasts in the rocks, or the crust there is so disrupted that no coherent scattering signals are reflected. We can exclude a high scattering near the surface as a reason, because between 14 and 19 km in length there are strong reflections from a depth between 6 and 10 km, which appear broadband and well structured. This speaks against attenuation of the wave energy. We have also verified this by comparing the reflection amplitudes on raw data inside and outside the transparent zone. Therefore, we interpret the poor reflectivity as a lack of distinct impedance contrasts. At a distance of 20 km, the transparent section coincides with the Siegen thrust system and the East Eifel Nappe. At a distance of 80 km, it coincides with the NPZ and appears to cover the entire crustal layer. Strain analyses confirm that the NPZ, as well as the Siegen thrust region, have accommodated considerable shear motion and have therefore been described as vertical ductile zones (Oncken et al., 1999). Interestingly, the reflective bands in the lower crust in the block south of the transparent zones are tilted to the north (dashed green lines in Figure 4) as expected for a formerly northward subducting lower crustal layer.

Although the depth of the Moho is not well defined in the two transparent sections of the lower crust from 82 to 88 km and from 15 to 26 km horizontal distance, it is clear that the Moho undergoes significant rise of about 2 km to the north over each section, each from a level of ~31 to 29 km depth. Between the two zones, the Moho level gradually recovers to its normal depth of 31 km. At the 0 km distance at the northern end of the DEKORP 1B profile, the Moho has again gradually reached 31 km depth, which is confirmed by comparison with the southern end of the reprocessed section of DEKORP 1A (Figure SC2, depth interval 29–31 km corresponds to ~9.8–10.4 s two-way-traveltime in the time-migrated section). A Moho depth of ≈29 km was independently indicated at profile distance 18 km from the crossing refraction seismic profile (Mechie et al., 1983, see Figure 4), although the zone below from 30–36 km depth showed unusually low *P* wave velocities. If we project the center of uplift, the mineral springs, and CO_2 mofettes in the Eifel along the trend of the reflection profile (Figure 4), they are concentrated in the segment of the lower crustal transparent zone and Moho offset below the Siegen thrust.

Within the transparent zone above the Moho step at 20 km distance and just north of the Siegen thrust at about 16 km distance, at the horizontal position of the Kelberg magnetic high, a prominent bright spot is visible at a depth between 6 and 10 km. The Kelberg high is located in the center of the Tertiary HEVF and has been explained by a combination of induced and remanent magnetized rocks at the top of a Tertiary upper crustal magma reservoir (Pucher, 1992). The reprocessing of DEKORP 1B allows to analyze the fine structure of the bright spot and to delineate the roof area of a differentiated reservoir in the upper and middle crust. Figure 5 shows a zoomed section of the Kelberg bright spot. Several highly reflective bands with a horizontal length of 2–4 km are visible. The highly reflective bands indicate a sequence of thin layers with strong impedance contrasts. For example, when thin layers act as a barrier to the rise of fluids, the accumulation of fluids under the seal layers generate a high impedance contrast, since the *P* and *S* wave velocities in the saturated, fractured, or porous layer under the seal are decreased. Such a fluid-related interpretation is well established for bright spots observed in sediments but also in crystalline crust (e.g., ANCORP Working Group, 2003). If the signal quality of the reflections is high and already visible in single shots, the investigation of amplitude versus offset (AVO) or the analysis of polarity changes in the reflecting bands can detect the presence of fluids in a bright spot. For DEKORP 1B the quality of the single shots is not sufficient for an AVO analysis of the true amplitudes. However, polarity reversals in single reflections of the Kelberg bright spot are indicated in single prestack depth-migrated traces (Figure 5). They cannot easily be traced

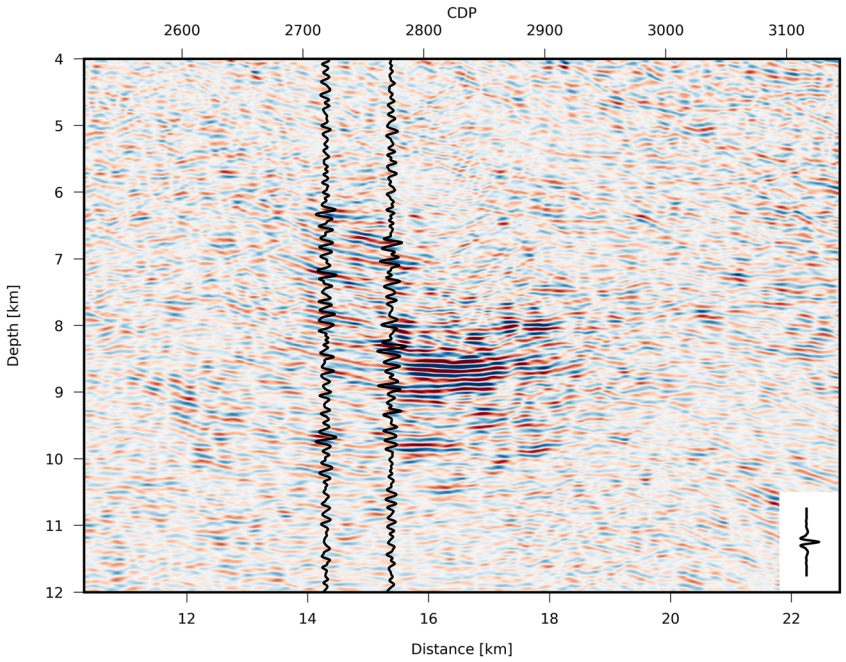

Figure 5. Prestack depth-migrated section zoomed to the KB bright spot (see Figure 4 for location). Colors indicate relative amplitudes, and two overlaid traces indicate polarity convention (positive wiggle to the right = red). The legend shows the incorporated average zero phase wavelet determined within the depth range of the KB bright spot.

along reflections, possibly because the distance between high and low impedance layers is so small that tuning effects obscure the patterns.

4. Discussion

Mush zones growing in the lower crust generate low degrees of derivative melts of intermediate compositions. For instance, the lava erupted in the youngest maar (Ulmener Maar) of the WEVF has 6.3 wt% MgO and an Mg# of 65 indicating a slightly differentiated magma composition, which is possibly derived from a mafic magma generated by very low degrees of partial melting (Schmincke, 2007). During the Moho-level, underplating intrusion period, the temperature in the upper crust does not change significantly (Karakas et al., 2017). As buoyant melts accumulate more and more in thin lenses within the lower-crust mush reservoir, melts and crystals may migrate upward to form upper-crustal mush reservoirs of highly evolved, differentiated magmas as, for instance, the strongly evolved Laacher See phonolites developed largely within Devonian slates and sandstones at 3–6 km depth (Wörner & Schmincke, 1984) or 5–6 km depth (Harms et al., 2004). Reactive melt flow is suggested as an efficient mechanism to form high-melt-fraction layers without a significant increase in temperature (Jackson et al., 2018). The lower-crust mush system impacts the storage conditions of upper-crustal reservoirs, and upper-crustal reservoirs may survive in a cold mush state for periods of 1 Ma or longer (Karakas et al., 2017). The mush concept could integrate the different observations compiled in this study, such as the anomalous sub-Moho v_P transition layer, the reduced velocity and transparent zone in a wedge-shaped zone in the lower crust beneath the WEVF, the depth and location of the Kelberg and Laacher See upper crustal reservoirs, the distribution of mineral springs containing mantle-derived CO_2, and the occurrence of DLF earthquakes in persistent clusters.

4.1. Anomalies Along the NE-SW Trending Refraction Seismic Profile 1979

The refraction seismic studies by Mechie et al. (1983) resolved a ≈6 km thick low-velocity gradient layer below 30 km depth (Figure 3). The profile crossed the Quaternary and Tertiary volcanic fields of the Eifel and Westerwald, and its trend is parallel to the suture zones and structures of the RHM and samples especially the crust beneath the Siegen thrust system and the Eifel nappe. In Figure 6 we plot the *P* wave velocities at the LSV (0 km in Figure 3) together with other parameters, such as the observed depth range of

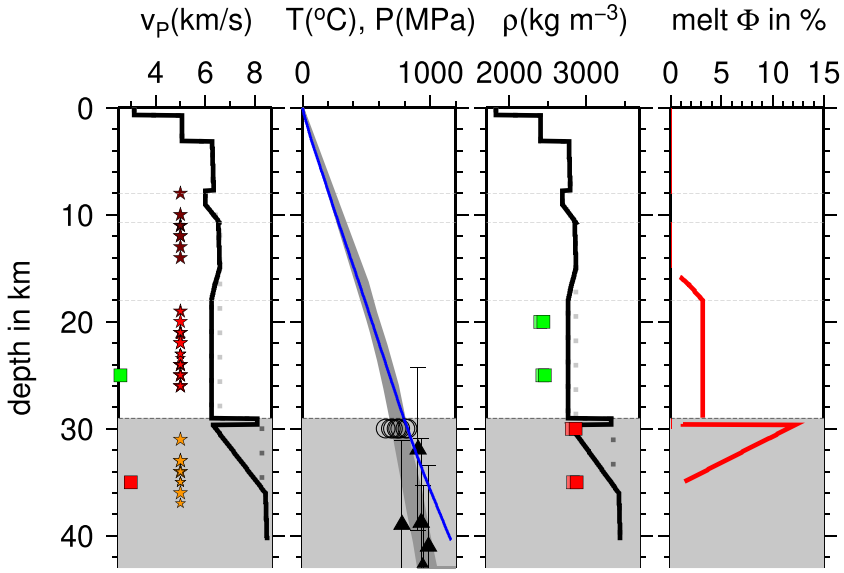

Figure 6. *P* wave velocity (v_P), temperature (T, gray band) and ambient pressure (P, blue line, same scale), density (ρ), and predicted melt fraction (in %) are plotted as a function of depth. The depths of DLF earthquakes between 2013 and 2019 are indicated by colored stars plotted in the left panel. The squares show predicted melt velocity and melt density (method of Ueki & Iwamori, 2016) of basanitic magma at 1000°C (red-filled, probe 1002-1 in Table 1 of Schmincke et al., 1983) and phonolitic magma at 800°C (green-filled, probe E 314 in Table 1 in Schmincke et al., 1983). The temperature (gray band) shows a model calculation for a measured surface heat flow between 80 and 90 mW/m^2 (see Witt-Eickschen, 2007). Symbols show z(P)-T estimates for equilibrated WEVF xenoliths (Witt-Eickschen, 2007). The pressure model (blue line) has been integrated from the bulk density model, which is based on t (vP) using the empirical relationship of Knopoff (1967). The dotted lines indicate the melt free reference model for vP and ρ which was used to calculate the melt fraction Φ to explain the low-velocity anomalies. An aspect ratio of 0.01 (Takei, 2002) was used for the calculation.

DLF earthquakes; estimates of temperature, pressure, and densities with depth; and an estimate of melt fraction in the low-velocity layers beneath the Moho and in the lower crust.

The temperature (T) was estimated by Garcia-Castellanos et al. (2000) for a measured heat flow of 80–90 mW/m^2, and compares well to T ranges derived from upper mantle xenoliths between 30 and 40 km depth (Figure 6, data from Witt-Eickschen, 2007). The T profile and the velocity-derived densities are used to predict velocities and densities of phonolitic (800°C) and basanitic melts (1000°C) at different depths above and below the Moho (Figure 6, method by Ueki & Iwamori, 2016, see supporting information S1).

In the lower crust and upper mantle, the velocity profile shows two low-velocity layers. They range along the Siegen thrust system from the WEVF to the EEVF and further to the WF, thereby crossing the Ulmener Maar and Laacher See. Both anomalies are most enhanced in their centers just beneath the Laacher See where also upwelling Moho is indicated, and they reach the shallowest levels at a distance of 0 in Figure 3. If low v_P would correlate with temperature, this could indicate that the thermal anomaly in the lower crust is largest beneath the Laacher See. The DEKORP line crossing the refraction line at the position of the Ulmener Maar has a transparent lower crust in the refraction-derived low v_P range. As seen in Figure 6, the lower crust velocities between 17 and 29 km depth are unusually small at ≈6.25 km/s, while velocities at 15 km depth reach almost 6.6 km/s. Table SA1 shows measured velocities for different rock types (Stadtlander et al., 1999) at temperatures and pressures associated with about 27 km depth. Felsic rocks such as schist, gneiss, granite, but also basalt, would explain the low velocities. The smallest Mesozoic lower crust velocities in the compilation of Behn and Kelemen (2003) can have $v_p \approx 6.3$ km/s. However, the structures seen in the crossing reflection seismic profiles suggest that the presence of metamorphosed sediments are not very likely at a depth of 27 km. For instance, granites have been assumed in the transparent section beneath the Saar-Nahe Half-Graben at depth ranges between 8 and 12 km, where larger velocities are observed in the refraction seismic line. Anhydrous granites, for instance related to a plutonic intrusion in

the lower crust from below, would generate low v_p/v_s ratios of 1.63 (Sobolev & Babeyko, 1994). Interlayering of mafic intrusions in igneous rocks, e.g., basalt (6.05–6.3 km/s) and gabbro (6.6 km/s at 28 km, Table SA1), would generate only slight variations in v_p velocities of laminated lower crust. Additionally, the lower crust v_P anomaly zone beneath the Ulmener Maar is nonreflective and transparent in the crossing DEKORP line, rendering a laminated lithology unlikely. Alternatively to lithology, the 5% reduced velocities compared to $v_p \approx 6.6$ km/s in 15 km depth may be explained by partial melts of about 3% (Figure 6, assuming phonolitic melts at 800°C and an aspect ratio of $\alpha = 0.01$, see Takei, 2002, and supporting information S1).

We interpret the Moho below the Laacher See at 29 km depth. The sub-Moho v_P anomaly is characterized by a sharp decrease at 30 km depth to 6.4 km/s, followed by a smooth increase to 8.1 km/s at 35 km depth. While 8.1 km/s is a typical mantle velocity, the low values of 6.4 km/s are unusual and may in terms of lithology represent basalt, metagabbro, diorite, granulite, amphibolite, or gneiss (Table SA1). Alternatively, a partially molten mantle with up to ≈10% melt directly below the Moho may explain the observed velocities (Figure 6, where we assumed basanitic melts at 1000°C and an aspect ratio of $\alpha = 0.01$, see Takei, 2002, and supporting information S1). As the velocities are gradually increasing from 30 to 35 km depth, a hydrostatic porosity model controlled by overpressure build-up beneath the crust-mantle boundary may explain the v_P gradient. If the saturated fluid would be CO_2 instead of basanitic melts, the fluid fraction would be much smaller. However, such a gas bearing layer would likely be recognized in the reflection seismics, which is not observed beneath the Ulmener Maar. If the segment between 30 and 35 km depth would be dominated by metamorphized crustal rocks, the melt fraction would be smaller at 3% or less. However, xenoliths from the shallow lithospheric mantle (Witt-Eickschen, 2007; see also Figure 6) hosted between 30 and 43 km depth do not confirm crustal rock contamination, indicating that the melts at this depth were hosted in upper mantle rocks.

There are three possibilities to explain the thin high-velocity layer between 29 and 30 km depth. Either it is the remnant of pristine upper mantle left after the region below between 30 and 35 km depth was invaded by partial melts and fluids (Mechie et al., 1983) or it is an intrusion into preexisting lower crustal material. If the rocks below are metamorphosed crustal rocks, e.g., granulite, amphibolite, or gneiss, then it must be an intrusion. Alternatively, it may be explained by multipathing of waves in the southern and northern blocks of the Moho step indicated in Figure 4. However, the results from an earlier profile about 40 km south of the 1979 profile mean that multipathing of waves is perhaps an unlikely explanation for the thin high-velocity layer between 29 and 30 km depth. For this earlier profile, Mooney and Prodehl (1978) recognized, in addition to the Moho, a second velocity discontinuity at a depth of about 33 km in the uppermost mantle. However, because the station density along the earlier profile was less than that along the 1979 profile, Mooney and Prodehl (1978) derived a velocity of 7.7 km/s immediately below the Moho and thus did not require the existence of a low-velocity zone in the region down to about 33 km depth in the uppermost mantle.

Hrubcová et al. (2017) interpreted the structure beneath the Eger rift, another region in Europe exhibiting Quaternary volcanism, in terms of active magmatic underplating with the possible presence of 3–5% melt. The appearance of the wide-angle reflected phases in the seismic data from the Eger rift is, however, somewhat different from that of such phases from the Eifel. Also, the velocity structure is somewhat different with generally higher velocities around the crust-mantle transition region beneath the Eger rift than under the Eifel.

The DLF earthquakes occur along a subvertical, channel-like path connecting the assumed location of the Laacher See magma reservoir with the center of the upper mantle low-velocity gradient layer (Figure 3). DLFs have been postulated to indicate locations of partial melt reservoirs, which are pressurized by the influx of magmatic fluids. Although the earthquakes are not exclusively associated with the low-velocity regions in the velocity model, the upper DLF earthquake cluster, twice active in April 2015 and in October 2018, begins at about the same depth, 8 km, as that where the uppermost low-velocity region starts (Figure 6). The middle earthquake cluster (active in June 2017 and in April 2018) fits quite nicely into the low-velocity region in the lower crust, between 17 and 29 km depth. The lower earthquake cluster (October 2017, May and June 2018, August and October 2019) also begins close to the top of the low-velocity zone in the transition region, below the thin high-velocity layer between 29 and 30 km depth. Two DLF mantle earthquakes, which occurred in September 2013 and mark the first observation of DLF

earthquakes in the Eifel after the local seismic network had been improved, extend throughout the low-velocity zone in the transition region and even into the region where normal upper mantle velocities in excess of 8 km/s are encountered at depths greater than 35 km.

4.2. Anomalies Along the NS Trending DEKORP 1B Profile

The Bouguer gravity anomaly (Figure 2c) shows elongated bands of positive and negative anomalies that run from NE-SW in the direction of major thrusts (e.g., Siegen thrust in the WEVF) and subparallel to the suture at the NPZ. They are not associated with superficial sediments (e.g., the Saar-Nahe Basin and the Neuwieder Becken) and must be generated by density variations in the crust. The Bouguer depressions up to −12 mGal cover the EEVF and WEVF and cannot be explained by the Moho step found in the reflection seismic data. An isostatically uncompensated Moho step would produce a Bouguer high at the centers of the volcanic fields, and the transition distance (in NW direction) from high to low would have an extension of more than 70 km, which is not observed. This suggests that the ribbon-like Bouguer anomalies originate in the lower and/or upper crust. Gravity modeling could test whether for instance a hot lower crust could help explain the Bouguer anomaly. For example, the gravity low in the active volcanic area of Campania, Gulf of Naples, which is assumed to be generated by a large mush reservoir with reduced density and a melt content of 30% and a lateral extent of about 50 km in the lower crust between 8 and 24 km depth, causes a gravity low of −30 mGal (Fedi et al., 2018).

Similar to the bands of these positive and negative anomalies, structural anomalies show a NE-SW trend subparallel to the strike of the refraction seismic profile and orthogonal to DEKORP 1. The DEKORP 1B profile crosses the refraction profile at the level of the Quaternary Ulmener Maar of the WEVF, and runs directly over the transparent zone, which has been interpreted as a possible hot zone that may contain partial melts. Such a hot zone would also explain the tectonic shearing and increased ductility found from the tectonic strain analysis (Oncken et al., 1999). According to the mush reservoir model, the structure of a reservoir in the middle or lower crust is complex. It has an overall thickness of several kilometers, but only thin layers at the top develop high-melt fractions, while the underlying mushy layers have low-melt fractions (Annen et al., 2006; Jackson et al., 2018). Such a structure impacts the geophysical signature of the reservoirs. For example, the wave energy reflected from a 200 m thick sill or dike of high-melt fraction is small and may not be detectable if the wave frequencies are less than 10 Hz. However, a several kilometer thick, hot, low-melt zone has probably healed lithological or tectonic impedance contrasts and will appear as a transparent zone in reflection seismic surveys.

The correlation of various parameters with the position of the wedge-shaped transparent zone can help to clarify its nature. For instance, the Quaternary uplift of the Eifel has its peak just in between the EEVF and WEVF on top of the presumed Moho step and the wedge-shaped lower crustal zone (Figure 7a). Mantle upwelling, and thus temperature and partial melt content, may be high in the region of highest uplift. The number of volcanoes in the EEVF and WEVF, projected along the NE-SW trend, is highest above the wedge-shaped transparent zone (Figure 7a). The diffuse degassing of CO_2 in springs and mofettes of Quaternary volcanic fields of the Eifel, and their He^3/He^4 and $\delta^{13}C_{CO2}$ isotopes, point to a predominantly mantle-derived origin of magmas (Bräuer et al., 2013). The distribution of CO_2 springs may indicate the regions of reservoirs and ongoing magmatic underplating at Moho level and in the lower crust. In Figure 7a we project the density of CO_2 springs for a ±20 km wide stripe crossing the WEVF and EEVF onto profiles subparallel to DEKORP 1B (similar to the trend of σ_1). Interestingly, the rate function has a similar shape for both fields, and the peak values correlate with the wedge-shaped transparent zone in the lower crust and the Moho step.

Geochemical variation of volcanic products in the WEVF may further support the model of a hot and weak lower crustal wedge close to the center of the volcanic fields. For instance, the crustal wedge may facilitate the upward migration of magma batches from the mantle, less affected by crustal contamination. MgO wt% is viewed as a measure for magma differentiation. In the WEVF, the MgO content is lowest above the transparent zone (Figure 7a, data from Mertes, 1983, see also Mertz et al., 2015), indicating a relative abundance of differentiated compared to primitive magmas. A similar conclusion was drawn by Schmincke et al. (1983) for the EEVF.

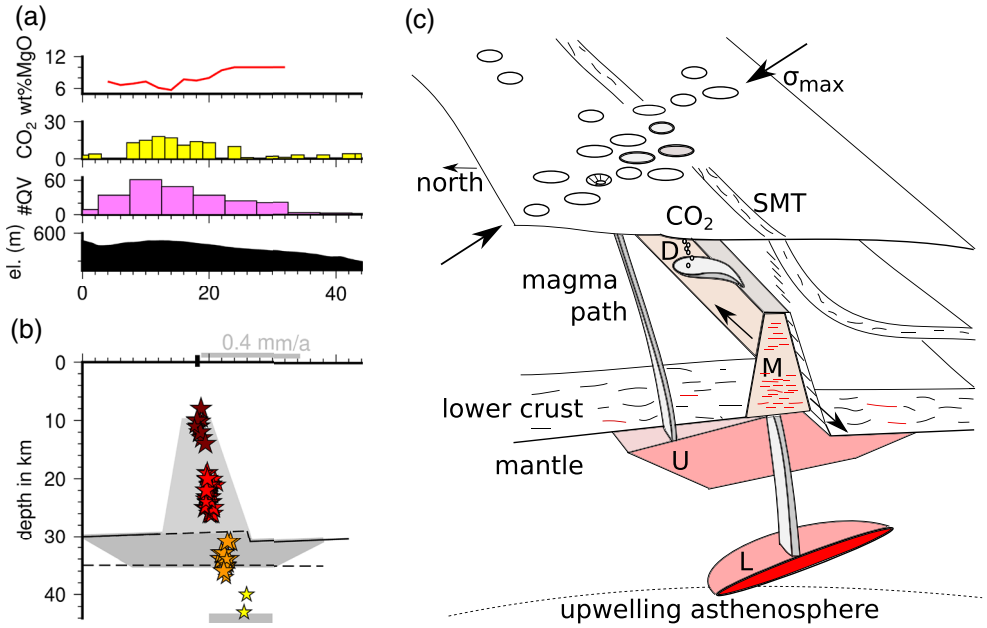

Figure 7. (a) Correlation of various parameters to the position of the wedge-shaped transparent zone and Moho offset estimated from DEKORP 1B (see Figure 4). Panels on top show the elevation, the numbers (#) of Quaternary Volcanoes from EEVF and WEVF, the number of CO_2 bearing mineral springs (separated for EEVF and WEVF), and the average wt% of MgO (data from Mertes, 1983). (b) DLF earthquakes from the EEVF (colored stars) are projected onto the crustal section. The gray bar on top indicates the region of maximum uplift. (c) Synthetic sketch. Proposal for a wedge-shaped Moho mushy reservoir (U + M) along the ductile zone of the Siegen Main thrust (SMT) feeding volcanism in the WEVF, EEVF, and WF. Decompression melting in the upper mantle (L) may be the source of basanitic melts, but their distribution to the surface is controlled by magmatic-tectonic processes rather than a single plume. Feeder channel from the mushy reservoirs to an upper crustal reservoir (D) is indicated.

Magnetotelluric methods have been successfully used to characterize zones of partial melt in the crust beneath volcanoes. For example, Didana et al. (2014) conducted a broadband magnetotelluric survey (0.003–1,000 s, 22 stations, 1 km distance) over the magmatic segment of Manda Hararo within the Tendaho Graben in the Afar depression in northeastern Ethiopia, where significant magmatic eruptions occurred between ~1.8 and ~0.6 Ma. They identified a highly conductive zone of 3–10 Ωm below the graben, which was interpreted as a shallow magma reservoir with ~13% partial melting between 5 and 8 km depth over a horizontal width of ~15 km. Jödicke et al. (1983) performed four magnetotelluric profiles (5–130 and 130–3,000 s; 70 stations with 5–15 km distance, 4 weeks duration) in the RHM perpendicular to the main trend of the Variscan fold belt (green lines in Figure 1). No differences in conductivity were found at an upper mantle depth of 50 km west and east of the Rhine. For a profile just in between the WEVF and EEVF, a well-conductive (~4–10 Ωm) intracrustal layer of ~5 km thickness and ~80 km length was found. Projected on the DEKORP1 profiles, it rises below the center of the WEVF to a depth of ~15 km and falls south to a depth of about 22 km north of the Boppard Thrust (BT in Figure 4). The increased conductivity was explained by Jödicke et al. (1983) by graphite layers or permeable fluid zones. Partial melt was identified as another possible cause for the high conductivity of the layers, but was rejected because of the assumed low temperatures in the middle crust.

The DEKORP 1B profile runs directly over the Kelberg magnetic high, which was interpreted as a residual Tertiary magma reservoir in the upper crust with subhorizontal sills at its top between 6.5 and 10 km depth. The roof zone of the reservoir appears as a bright spot in the depth-migrated section, perhaps due to CO_2 and/or hydrous fluids below the solidified sills. The depth range of the Kelberg bright spot is similar to the depth range of the Laacher See chamber as constrained by geochemical studies on volcanic products from the 12.9 ka Plinian Laacher See eruption. The Tertiary Kelberg reservoir could therefore be a model for the active reservoir beneath the Laacher See of today. It is then interesting to project the DLF earthquakes from the EEVF along the NE-SW trend of the Siegen thrust onto the DEKORP 1B depth section.

The DLFs align along the slope of the southern border of the transparent zone as identified in the reflection seismics (Figure 7b). The upper level of the DLFs is at the depth level of the Kelberg bright spot. This agreement suggests that the geometry of the ascent paths for magmatic fluids and the depth extension of a differentiated magma reservoir in the upper crust under the EEVF are similar to those under Kelberg in the Western Eifel. However, a magnetic anomaly similar to that at Kelberg is not observed at the Laacher See.

In summary, various parameters correlate with the structure of the crust-mantle boundary (Figure 7b) and especially the Moho offset beneath the Siegen thrust zone at the WEVF, which strikes in the same direction as the tectonic lineaments and the refraction seismic line from 1979. As the sub-Moho velocity anomaly identified in the refraction seismic data has a lateral extent of more than 100 km, reaching from the WEVF to the WF, the Moho offset and the transparent lower crustal wedge may be larger structural elements of similar extension.

4.3. Interpretation

Interestingly, the Quaternary and most of the Tertiary volcanic fields of the RHM align subparallel to the NPZ (Figures 1 and 2a) located about 60–100 km to the SE, which shows a Moho step and represents a lithospheric terrane boundary from the Variscan collision and the subduction of the Rheic (and Rheno-Hercynian) ocean (Franke et al., 2017; Koenigshof et al., 2016). In the past, a flat subduction of the oceanic lithosphere (e.g., Axen et al., 2018; Li & Li, 2007) led to the formation of a compressional thrust and fold belt in the RHM, displacing the lowermost portion of the continental Rheno-Hercynian lithosphere, which accumulated in a growing keel ahead of the slab. This may have led to the intrusion of granitic plutons at the position of the transparent zone of the Kelberg bright spot and a Moho step in the backarc of the former suture zone. After foundering or removal of the flat slab, the fossil keel may still drift in the upper mantle and be recognized by *S* wave velocity anomalies. The solidus of the asthenosphere and lithosphere was locally lowered by the infiltration of slab-derived hydrous fluids. Rebound of the former slab (e.g., Magni et al., 2017), or the upwelling of the asthenospheric and lithospheric mantle since the Tertiary, e.g., supported by the Alpine collision, leads to adiabatic decompression melting and the uplift of the RHM. Systems of overthrusting in the former backarc range represent structural weaknesses and appear to control the location of volcanic fields, such as the Siegen thrust for the WEVF and EEVF and the Eisenroth thrust between the Hörre anticline and Dill syncline at the Westerwald field in the east.

Figure 7c shows a synoptic volcano-structural summary of the reservoir model beneath the Quaternary fields of the Eifel. Melt today accumulates in upper mantle reservoirs (L in Figure 7c) beneath the weakened lithosphere and along the full segment of the Moho step (U in Figure 7c). The upper mantle reservoirs occasionally release batches of primary, primitive magmas which migrate into the crust and generate the anorogenic, dominantly alkaline volcanic provinces in the RHM (note that in the EEVF distinct groups of sodic-potassic alkaline rocks were erupted, too). Most of the intrusions entering the lower crust remain there as sills, and alter the lower crust by underplating. The weakened crust at the Moho step may act as a zone where intrusions can more easily reach higher levels and more channelized flow of magmatic fluids is supported. The ductile zone has heated up with time and represents in its lower part a mush-type lower crustal reservoir (M in Figure 7c). The mush zone is identified in the reflection seismic sections as a broad transparent zone beneath KB, and the Moho transition is smeared out and not sharp across these segments so that it is not visible in reflection seismics. The CO_2 flux has its highest concentration above the transparent zone. The channelized migration of magma through the lower crust and upper mantle leads to DLF earthquakes when small pockets/layers of differentiated melt are hit and receive influx of hot primary melt. It also favors the continuous recharge of upper crustal sill intrusions, so that differentiated, phonolitic melt reservoirs can develop in the upper crust. The Kelberg bright spot is one example.

Our results fit smoothly into the concepts of anorogenic plateau formation developed by Duesterhoeft et al. (2012), Li and Li (2007), or Axen et al. (2018), and anorogenic alkaline volcanism and Cenozoic magmatism within Europe to the north of the Alpine collision zone (e.g., Wilson & Downes, 2006). According to Wilson and Downes (2006), the east-west elongated terrane boundaries of microcontinent collision during the Variscan form regions of anomalously thin, irregular, or weak lithosphere and have exerted a significant control on the location of subsequent Cenozoic magmatism. They act as pathways for magma ascent through the lithosphere. Independent of the details of the processes leading to partial melting in the asthenosphere,

the Variscan structural fabric has preconditioned the subsequent locations of the Tertiary and Quaternary volcanism in the RHM.

The findings of this paper help to plan analysis studies and to design future experiments to better image and characterize the magmatic reservoirs and the plumbing system beneath the Quaternary volcanic fields of the Eifel. For instance, postulating that the DLF earthquakes beneath the Laacher See indicate the position and shape of the channel feeding the upper crustal magma reservoir beneath the Laacher See, the comparison with the Kelberg bright spot indicates the target depth and the strike and lateral extent that can be expected beneath the Laacher See. Interestingly, the expected depth, orientation, and length are in good agreement with the distribution of the swarm of microearthquakes (so-called Glees 2017 swarm, Hensch et al., 2019), which occurred in the upper crust immediately after the occurrence of the most energetic DLF burst observed so far. Imaging the wedge-shaped zone in the lower crust and below the Moho would need other approaches and techniques. Here ambient noise surface wave studies along perpendicular profiles may detect reduced *S* wave velocities in the wedge, enhanced amplitude attenuation for waves traveling along the trend of the ST system, and may also resolve a possible directional anisotropy. Short-period Rayleigh and Love waves have the potential to identify radial anisotropy, which could indicate fine horizontal layered melt bodies (e.g., Jaxybulatov et al., 2014; Jiang et al., 2018). In rare cases, active seismic shear wave experiments have been used to unravel the nature of the Variscan, laminated lower crust (Rabbel et al., 1998).

The model is important to assess the volcanic hazard, but has also potential consequences for the understanding of the spatial distribution of seismic hazard. Historic catalogs document a lack of $M > 5.1$ earthquakes in the Middle Rhine segment of the Rhine graben between Bingen and Bonn, while larger earthquakes occurred to the south and north. This uneven distribution of seismic hazard may be related to the presence of a NE-SW trending zone of weakened lower crust, which can support ductile behavior and limit the effective shear stress build up in the crust.

5. Conclusion

We reprocessed steep-angle reflection seismic profiles crossing the Quaternary and Tertiary Eifel volcanic fields and compiled various observations from geophysics, seismology, fluid geochemistry, and isotope studies that indicate the depth, distribution, and character of the magmatic reservoirs under the volcanic fields of the RHM. The complementary data suggest that Cenozoic volcanism in the Eifel and Westerwald is controlled by northeast-southwest running Variscan terrane boundaries marking a lithospheric zone of weakness. The zone is characterized by a Moho offset of ≈2 km. A 5–6 km thick, low-velocity gradient layer is present over a distance of nearly 120 km below this zone. If this gradient layer is caused by partial melts, the melt content from the bottom of the layer to the Moho increases from 0% to about 10%. The lower crust above the gradient layer has unusually small *P* wave velocities of only 6.25 km/s, which may be associated with anhydrous felsic rocks of high temperature or mafic igneous rocks of the lower crust and the presence of ≈3% partial melts. The Moho depth indicates a small upwelling, and the reduction in velocity in the lower crust is greatest where the Moho is shallowest. DLF earthquakes originate at 43 km depth in the mantle just below the center of the anomalous low-velocity gradient layer, and from there follow a channel-like path toward the youngest volcanic center in the East Eifel, the Laacher See. A crossing reflection seismic profile shows that the low-velocity layer in the lower crust correlates with a transparent, wedge-shaped zone lacking reflection energy. A bright spot sits on top of the transparent zone and is interpreted as a residual magmatic reservoir of the Tertiary Hocheifel field. Supported by the correlation of various geophysical, fluid-geochemical, and volcanological observations, we suggest that the low-velocity layers in the upper mantle and lower crust can concentrate melts and magmatic fluids also at the present-day.

Data Availability Statement

The data for the 1978/1979 seismic refraction profiles were obtained from the Geophysical Instrument Pool Potsdam (GIPP) Experiment and Data Archive (DOI data publication via GFZ Data Services, Mechie et al., 2020).

Acknowledgments

We thank Karin Bräuer for discussion of isotope fluid components. TD thanks Susanne Köster for help during the preparation of the manuscript and editing tables and Jan Bergmann Barrocas (LIAG) for help preparing plots. The constructive comments of three reviewers helped to improve the manuscript. We thank the DEKORP archive (DOI data publications via GFZ Data Services, Stiller et al., 2020a, 2020b, 2020c) for access to the data of profiles and the Geological Survey of Rhineland-Palatinate for funding the reprocessing of the DEKORP 1B and 1C. We thank the Geological Survey of North Rhine-Westphalia and DMT GmbH & Co KG for the support and funding of the reprocessing of DEKORP 1A. The paper is related to activities in the PoF-IV programme Topic 3 of GFZ.

References

Aeschbach-Hertig, W., Kipfer, R., Hofer, M., Imboden, D. M., Wieler, R., & Signer, P. (1996). Quantification of gas fluxes from the sub-continental mantle: The example of Laacher See, a maar lake in Germany. *Geochimica et Cosmochimica Acta*, *60*(1), 31–41. https://doi.org/10.1016/0016-7037(95)00370-3

ANCORP Working Group (2003). Seismic Imaging of a convergent continental margin and plateau in the central Andes (ANCORP'96). *Journal of Geophysical Research*, *108*(B7), 2328. https://doi.org/10.1029/2006jb004431

Anderson, D. L. (1998). The helium paradoxes. *Proceedings of the National Academy of Sciences (USA)*, *95*(9), 4822–4827. https://doi.org/10.1073/pnas.95.9.4822

Annen, C., Blundy, J. D., & Sparks, R. S. J. (2006). The genesis of intermediate and silicic magmas in deep crustal hot zones. *Journal of Petrology*, *47*(3), 505–539. https://doi.org/10.1093/petrology/egi084

Axen, G. J., van Wijk, J. W., & Currie, C. A. (2018). Basal continental mantle lithosphere displaced by flat-slab subduction. *Nature Geoscience*, *11*, 961–964. https://doi.org/10.1038/s41561-018-0263-9

Behn, M. D., & Kelemen, P. B. (2003). Relationship between seismic P-wave velocity and the composition of anhydrous igneous and meta-igneous rocks. *G-Cube*, *4*(5), n/a. https://doi.org/10.1029/2002GC000393

Bekaert, D. V., Broadley, M., Caracausi, A., & Marty, B. (2019). Novel insights in the degassing history of Earth's mantle from high precision noble gas analysis of magmatic gas. *Earth and Planetary Science Letters*, *525*, 115766. https://doi.org/10.1016/j.eps2019.115766

Bogaard, P. J. F., & Wörner, G. (2003). Petrogenesis of basanitic to tholeiitic volcanic rocks from the Miocene Vogelsberg, Central Germany. *Journal of Petrology*, *44*(3), 569–602.

Brauer, A., Endres, C., & Negendank, J. F. (1999). Lateglacial calendar year chronology based on annually laminated sediments from Lake Meerfelder Maar, Germany. *Quaternary International*, *61*(1), 17–25. https://doi.org/10.1016/S1040-6182(99)00014-2

Bräuer, K., Kämpf, H., Niedermann, S., & Strauch, G. (2013). Indications for the existence of different magmatic reservoirs beneath the Eifel area (Germany): A multi-isotope (C, N, He, Ne, Ar) approach. *Chemical Geology*, *356*, 193–208. https://doi.org/10.1016/jchemgeo.2013.08.013

Büchel, G. (1990). Das Kelberger Hoch – Ein integriertes Modell einer tertiären Magmakammer. *Habilitationsschrift, Institut für Geowissenschaften* (pp. 1–142). Germany: Universität Mainz.

Budweg, M., Bock, G., & Weber, M. (2006). The Eifel Plume—Imaged with converted seismic waves. *Geophysical Journal International*, *166*(2), 579–589. https://doi.org/10.1111/j.1365-246X.2005.02778.x

DEKORP Research Group (1991). Results of the DEKORP 1 (BELCORP-DEKORP) deep seismic reflection studies in the western part of the Rhenish Massif. *Geophysical Journal International*, *106*(1), 203–227. https://doi.org/10.1111/j.1365-246X.1991.tb04612.x

Didana, Y. L., Thiel, S., & Heinson, G. (2014). Magnetotelluric imaging of upper crustal partial melt at Tendaho graben in Afar, Ethiopia. *Geophysical Research Letters*, *41*, 3089–3095. https://doi.org/10.1002/201GL060000

Duesterhoeft, E., Bousquet, R., Wichura, H., & Oberhänsli, R. (2012). Anorogenic plateau formation: The importance of density changes in the lithosphere. *Journal of Geophysical Research*, *117*, B07204. https://doi.org/10.1029/2011JB009007

Fedi, M., Cella, F., D'Antonio, M., Florio, G., Paoletti, V., & Morra, V. (2018). Gravity modeling finds large magma body in the deep crust below the Gulf of Naples, Italy. *Scientific Reports*, *8*, 8229. https://doi.org/10.1038/s41598-018-26,346-z

Fekiacova, Z., Mertz, D. F., & Hofmann, A. W. (2007). Geodynamic setting of the Tertiary Hocheifel volcanism (Germany), Part II: Geochemistry and Sr, Nd and Pb Isotoic Compositions. In J. R. R. Ritter, & U. R. Christensen (Eds.), *Mantle Plumes, A Multidisciplinary Approach* (pp. 207–240). Heidelberg: Springer.

Förster, M., Zemlitskaya, A., Otter, L., Buhre, S., & Sirocko, F. (2020). Late Pleistocene Eifel eruptions: Insights from clinopyroxene and glass geochemistry of tephra layers from Eifel Laminated Sediment Archive sediment cores. *Journal of Quarternary Science*, *35*(1-2), 186–198. https://doi.org/10.1002/jqs3134

Franke, W. (2014). Topography of the Variscan orogen in Europe: Failed—Not collapsed. *International Journal of Earth Sciences (Geologische Rundschau)*, *103*(1), 1471–1499. https://doi.org/10.1007/s00531-014-1014-9

Franke, W., Cocks, L. R. M., & Torsvik, T. H. (2017). The Paleozoic Variscan oceans revised. *Gondwana Research*, *48*, 257–284. https://doi.org/10.1016/j.gr.2017.03.005

Fuchs, K., von Gehlen, K., Mälzer, H., Murawski, H., & Semmel, A. (1983). Epilogue: Mode and mechanism of Rhenish Plateau uplift. In K. Fuchs, et al. (Eds.), *Plateau Uplift* (pp. 405–411). Verlag Heidelberg: Springer.

Gabriel, G., Vogel, D., Scheibe, R., Lindner, H., Pucher, R., Wonik, T., & Krawczyk, C. M. (2011). Anomalies of the Earth's total magnetic field in Germany—The first complete homogenous data set reveals new opportunities for multiscale geoscientific studies. *Geophysical Journal International*, *184*(3), 1113–1118. https://doi.org/10.1111/j.1365-246X.2010.04924.x

Garcia-Castellanos, D., Cloetingh, S., & Van Balen, R. (2000). Modeling the Middle Pleistocene uplift in the Ardennes–Rhenish Massif: Thermo-mechanical weakening under the Eifel? *Global and Planetary Change*, *27*(1-4), 39–52. https://doi.org/10.1016/S0921-8181(01)00058-3

Griesshaber, E., Onions, R. K., & Oxburgh, E. R. (1992). Helium and carbon isotope systematics in crustal fluid from the Eifel, the Rhine Graben and Black-Forest, FRG. *Chemical Geology*, *99*(4), 213–235. https://doi.org/10.1016/0009-2541(92)90178-8

Haase, K. M., Goldschmidt, B., & Garbe-Schoenberg, C. D. (2004). Petrogenesis of Tertiary continental intra-plate lavas from the Westerwald region. *Journal of Petrology*, *42*(5), 883–905. https://doi.org/10.1093/petrology/eggl115

Harms, E., Gardner, J. E., & Schmincke, H. U. (2004). Phase equilibria of the Lower Laacher See Tephra (East Eifel, Germany): Constraints on pre-emptive storage conditions of a phonolitic magma reservoir. *Journal of Volcanology and Geothermal Research*, *134*(1), 125–138. https://doi.org/10.1016/j.jvolgeores.2004.01.009

Henk, A. (1993). Subsidenz und Tektonik des Saar-Nahe Beckens (SW-Deutschland). *Geologische Rundschau*, *82*, 3–19.

Hensch, M., Dahm, T., Ritter, J., Heimann, S., Schmidt, B., Stange, S., & Lehmann, K. (2019). Deep low-frequency earthquakes reveal ongoing magmatic recharge beneath Laacher See Volcano (Eifel, Germany). *Geophysical Journal International*, *216*(3), 2025–2036. https://doi.org/10.1093/gji/ggy532

Hinzen, K.-G. (2003). Stress field in the Northern Rhine area, Central Europe, from earthquake fault plane solutions. *Tectonophysics*, *377*(3-4), 325–356. https://doi.org/10.1016/j.tecto.2003.10.004

Hrubcová, P., Geissler, W. H., Bräuer, K., Vavrycuk, V., Tomek, C., & Kämpf, H. (2017). Active magmatic underplating in western Eger Rift, Central Europe. *Tectonics*, *36*, 2846–2862. https://doi.org/10.1002/2017TC004710

Jackson, M. D., Blundy, J., & Sparks, R. S. J. (2018). Chemical differentiation, cold storage and remobilization of magma in the Earth's crust. *Nature*, *564*(7736), 405–409. https://doi.org/10.1038/s41586-018-0746-2

Jaxybulatov, K., Shapiro, N. M., Koulakov, I., Mordret, A., Landès, M., & Sens-Schönfelder, C. (2014). A large magmatic sill complex beneath the Toba caldera. *Science*, *346*(6209), 614–617. https://doi.org/10.1126/science.1256785

Jiang, C., Schmandt, B., Farrell, J., Lin, F.-C., & Ward, K. M. (2018). Seismically anisotropic magma reservoirs underlying silicic calderas. *Geology*, *46*(8), 727–730. https://doi.org/10.1130/G45104.1

Jödicke, H., Untied, J., Olgemann, W., Schulte, L., & Wagenitz, V. (1983). Electrical conductivity structure of the crust and upper mantle beneath the Rhenish Massif. In K. Fuchs, et al. (Eds.), *Plateau Uplift* (pp. 288–302). Verlag Heidelberg: Springer. https://doi.org/10.1007/978-3-642-69219-2_33

Karakas, O., Degruyter, W., Bachmann, O., & Dufek, J. (2017). Lifetime and size of shallow magma bodies controlled by crustal-scale magmatism. *Nature Geoscience*, *10*(6), 446–450. https://doi.org/10.1038/NGEO2959

Keyser, M., Ritter, J. R. R., & Jordan, M. (2002). 3-D shear wave velocity structure of the Eifel plume, Germany. *Earth and Planetary Science Letters*, *203*, 58–82. https://doi.org/10.1016/s0012-821x(02)00861-0

Knopoff, L. (1967). Density-velocity relations for rocks. *Geophysical Journal of the Royal Astronomical Society*, *13*, 1–8. https://doi.org/10.1111/j.1365-246X.1967.tb02143.x

Koenigshof, P., Becker, R. T., & Hartenfels, S. (2016). The Rhenish Massif as a part of the European Variscides. *Münstersche Forsch Geol Palaeontol*, *108*, 1–13.

Korsch, R. J., & Schäfer, A. (1995). The Permo-Carboniferous Saar-Nahe Basin, south-west Germany and north-east France: Basin formation and deformation in a strike-slip regime. *Geologische Rundschau*, *84*(2), 293–318. https://doi.org/10.1007/s005310050007

Kreemer, C., Blewitt, G., & Davis, P. M. (2020). Geodetic evidence for a buoyant mantle plume beneath the Eifel volcanic area, NW Europe. *Geophysical Journal International*, *222*(2), 1316–1332. https://doi.org/10.1093/gji/ggaa227

Kurihara, R., Obara, K., Takeo, A., & Tanaka, Y. (2019). Deep low-frequency earthquakes correlated with the Eruptions of Shinmoedake in Kirishima volcano. *Journal of Geophysical Research*, *124*(12), 13079–13095. https://doi.org/10.1029/2019JB018032

Li, Z. X., & Li, X. H. (2007). Formation of the 1,300-km-wide intracontinental orogen and postorogenic magmatic province in Mesozoic South China: A flat subduction model. *Geology*, *35*, 179–182. https://doi.org/10.1130/G23193A.1

Lippolt, H. J. (1983). Distribution of volcanic activity in space and time. In K. Fuchs, K. von Gehlen, H. Mälzer, H. Murawski, & A. Semmel (Eds.), *Plateau Uplift* (pp. 112–120). Berlin-Heidelberg: Springer.

Lippolt, H. J., & Hess, J. C. (1989). Isotopic evidence for the stratigraphic position of the Saar-Nahe Rotliegende volcanism III. Synthesis of results and geological implications. *Neues Jahrbuch für Geologie und Paläontologie*, 553–559. https://doi.org/10.1127/njgpm/1989/1989/553

Magni, V., Allen, M. B., van Huenen, J., & Bouilhol, P. (2017). Continental underplating after slab break-off. *Earth and Planetry Science Lett.*, *474*, 59–67. https://doi.org/10.1016/j.epsl.2017.06.017

Marsh, B. D. (1989). Magma chambers. *Annual Review of Earth and Planetary Sciences*, *17*(1), 439–472. https://doi.org/10.1146/annurev.ea.17.050189.002255

May, F. (2002). *Quantifizierung des C02-Flusses zur Abbildung magmatischer Prozesse im Untergrund der Westeifel*, *Berichte aus der Geowissenschaft* (p. 170). Aachen, Aachen: Shaker Verlag. ISBN 3-8322-0224-2.

Mechie, J., Prodehl, C., & Fuchs, K. (1983). The long-range seismic refraction experiment in the Rhenish Massif. In K. Fuchs, K. von Gehlen, H. Mälzer, H. Murawski, & A. Semmel (Eds.), *Plateau Uplift* (pp. 261–274). Heidelberg: Springer Verlag.

Mechie, J., Prodehl, C., Fuchs, K., Kaminski, W., Flick, J., Hirn, A., et al. (1982). Progress report on the Rhenish Massif seismic experiment. *Tectonophysics*, *90*(1-2), 215–230. https://doi.org/10.1016/0040-1951(82)90263-3

Mechie, J., Prodehl, C., Kaminski, W., Fuchs, K. (2020): Data from the 1978–79 Rhenish Massif seismic refraction experiment. *GFZ Data Services*. http://doi.org/10.5880/GIPP.197901.1

Meissner, R., Bartelsen, H., & Murawski, H. (1980). Seismic reflection and refraction studies for investigating fault zones along the geotraverse Rhenohercynicum. *Tectonophysics*, *64*(1-2), 59–84. https://doi.org/10.1016/0040-1951(80)90262-0

Meissner, R., & Bortfeld, R. K. (1990). *DEKORP Atlas—Results of the Deutsches Kontinentales Reflexionsseismisches Programm*. Berlin, Heidelberg: Springer. https://doi.org/10.1007/978-3-642-75662-7

Mertes, H. (1983). Aufbau und Genese des Westeifeler Vulkanfelds. *Bochumer geol. u. geotechn. Arb*. (pp. 415). Bochum: Institut für Geologie der Ruhr Universität Bochum.

Mertz, D. F., Loehnertz, W., Nomade, S., Pereira, A., Prelevic, D., & Renne, P. R. (2015). Temporal-spatial evolution of low-SiO_2 volcanism in the Pleistocene West Eifel volcanic field (West Germany) and relationship to upwelling asthenosphere. *Journal of Geodynamics*, *88*, 59–79. https://doi.org/10.1016/j.jog.2015.04.002

Meyer, W., & Stets, J. (2007). Quaternary uplift in the Eifel area. In J. R. R. Ritter, & U. R. Christensen (Eds.), *Mantle Plumes – A Multidisciplinary Approach* (pp. 369–378). Heidelberg: Springer Verlag.

Mooney, W. D., & Prodehl, C. (1978). Crustal structure of the Rhenish Massif and adjacent areas; a reinterpretation of existing seismic-refraction data. *Journal of Geophysics*, *44*, 573–601.

Oncken, O., von Winterfeld, D., & Dittmar, U. (1999). Accretion of a rifted passive margin: The Late Paleozoic Rhenohercynian foild and thrust belt (Middle European Variscides). *Tectonics*, *18*(1), 75–91. https://doi.org/10.1029/98TC02763

Pfaender, J. A., Jung, S., Kluegel, A., Muenker, C., Romer, R. L., Sperner, B., & Rohrmüller, J. (2018). Recurrent local melting of metasomatised lithospheric mantle in response to continental rifting: Constraints from basanites and nephelinites/melilitites from SE Germany (2018). *Journal of Petrology*, *59*, 667–694. https://doi.org/10.1093/petrology/egy041

Pfiffner, O. A. (2017). Thick-skinned and thin-skinned tectonics: A global perspective. *Geosciences*, *7*(3), 71. https://doi.org/10.3390/geosciences7030071

Puchelt, H. (1983). Carbon dioxide in the Rhenish Massif. In K. Fuchs, K. von Gehlen, H. Mälzer, H. Murawski, & A. Semmel (Eds.), *Plateau uplift: the Rhenish Shield - a case history* (p. 152). Berlin, Heidelberg: Springer Verlag. https://doi.org/10.1007/978-3-642-69219-2_22

Pucher, R. (1992). Magnetfeldanomalien in der Eifel. *Geologische Rundschau*, *81*(2), 429–443. https://doi.org/10.1007/BF01828608

Rabbel, W., Siegesmund, S., Weiss, T., Pohl, M., & Bohlen, T. (1998). Shear wave anisotropy of laminated lower crust beneath Urach (SW Germany): A comparison with xenoliths and with exposed lower crustal sections. *Tectonophysics*, *298*(4), 337–356. https://doi.org/10.1016/S0040-1951(98)00174-7

Ritter, J. R. R. (2007). The seismic signature of the Eifel plume. In J. R. R. Ritter, & U. R. Christensen (Eds.), *Mantle Plumes – A Multidisciplinary Approach* (pp. 379–404). Heidelberg: Springer Verlag.

Ritter, J. R. R., Jordan, M., Christensen, U. R., & Achauer, U. (2001). A mantle plume below the Eifel volcanic fields, Germany. *Earth and Planetary Science Letters*, *186*(1), 7–14. https://doi.org/10.1016/S0012-821X(01)00226-6

Ritter, J. R. R., Mathar, J. P., Jordan, M., & Gabriel, G. (2007). Gravity observations in the Western Rhenish Massif and forward modelling of the Eifel Plume Bouguer Anomaly. In J. R. R. Ritter, & U. R. Christensen (Eds.), *Mantle Plumes – A Multidisciplinary Approach* (pp. 465–476). Heidelberg: Springer Verlag.

Rout, S. S., & Wörner, G. (2018). Zoning and exsolution in alkali feldspars from the Laacher See volcano (Western Germany): Constraints on temperature history prior to eruption. *Contributions to Mineralogy and Petrology*, *173*(11), 95. https://doi.org/10.1007/s00410-018-1,522-x

Schmincke, H. U. (2007). The Quaternary Volcanic Fields of the East and West Eifel (Germany). In J. R. R. Ritter, & U. R. Christensen (Eds.), *Mantle Plumes—A Multidisciplinary Approach* (pp. 241–322). Heidelberg: Springer Verlag.

Schmincke, H. U., Lorenz, V., & Seck, H. A. (1983). The Quaternary Eifel volcanic fields. In K. Fuchs, K. von Gehlen, H. Mälzer, H. Murawski, & A. Semmel (Eds.), *Plateau Uplift* (pp. 139–151). Heidelberg: Springer Verlag.

Schmitt, A. K. (2006). Laacher See revisited: High-spatial-resolution zircon dating indicates rapid formation of a zoned magma chamber. *Geology*, *34*(7), 597–600. https://doi.org/10.1130/G22533.1

Schmitt, A. K., Wetzel, F., Cooper, K. M., Zou, H. B., & Wörner, G. (2010). Magmatic longevity of Laacher See Volcano (Eifel, Germany) indicated by intrusive carbonatites. *Journal of Petroleum*, *50*, 1053–1085. https://doi.org/10.1093/petrology/egq011

Sebazungu, E. (2005). *Investigations on maar-diatreme volcanoes by inversion of magnetic and gravity data from the Eifel area, Germany. PhD thesis, Department of Chemistry* (pp. 1–180). Germany: Pharmaceutics and Geosciences of the Johannes Gutenberg University of Mainz.

Seck, A. H., & Wedepohl, K. H. (1983). Mantle xenoliths in the Rhenish Massif and the Northern Hessian depression. In K. Fuchs, et al. (Eds.), *Plateau Uplift* (pp. 261–274). Heidelberg: Springer Verlag.

Sobolev, S. V., & Babeyko, A. (1994). Modeling of mineralogical composition, density and elastic wave velocities in anhydrous magmatic rocks. *Surveys in Geophysics*, *15*(5), 515–544. https://doi.org/10.1007/BF00690173

Soosalu, H., Key, J., White, R. S., Knox, C., Einarsson, P., & Jakobsdóttir, S. S. (2010). Lower-crustal earthquakes caused by magma movement beneath Askja volcano on the north Iceland rift. *Bulletin of Volcanology*, *72*(1), 55–62. https://doi.org/10.1007/s00445-009-0297-3

Stadtlander, R., Mechie, J., & Schulze, A. (1999). Deep structure of the southern Ural mountains as derived from wide-angle seismic data. *Geophysical Journal International*, *137*, 501–515. https://doi.org/10.1046/j.1365-246x.1999.00794.x

Stiller, M., Kaerger, L., Agafonova, T., Krawczyk, Ch., Oncken, O., Weber, M., Former DEKORP Project Leaders; Former DEKORP Research Group; Former DEKORP Processing Centre (2020b): Deep seismic reflection profile DEKORP 1987-1B across the western Rhenish Massif, West Germany. GFZ Data Services. http://doi.org/10.5880/GFZ.DEKORP-1B.001

Stiller, M., Kaerger, L., Agafonova, T., Krawczyk, Ch., Oncken, O., Weber, M., Former DEKORP Project Leaders; Former DEKORP Research Group; Former DEKORP Processing Centre (2020c): Deep seismic reflection profile DEKORP 1988-1C across the western Rhenish Massif, West Germany. GFZ Data Services. http://doi.org/10.5880/GFZ.DEKORP-1C.001

Stiller, M., Kaerger, L., Agafonova, T., Krawczyk, Ch., Oncken, O., Weber, M., Former DEKORP Project Leaders; Former DEKORP/BELCORP Research Group; Former DEKORP Processing Centre (2020a): Deep seismic reflection profile DEKORP 1987-1A across the western Rhenish Massif, West Germany/East Belgium. GFZ Data Services. http://doi.org/10.5880/GFZ.DEKORP-1A.001

Takei, Y. (2002). Effect of pore geometry on VP/VS: From equilibrium geometry to crack. *Journal of Geophysical Research*, *107*(B2), 2043. https://doi.org/10.1029/2001JB000522

Trieloff, M., & Altherr, R. (2007). He-Ne-Ar isotope systematics of Eifel and Pannonean Basin mantle xenoliths trace deep mantle plume-lithosphere interaction beneath European continents. In J. R. R. Ritter, & U. R. Christensen (Eds.), *Mantle Plumes—A Multidisciplinary Approach* (pp. 339–368). Heidelberg: Springer Verlag.

Ueki, K., & Iwamori, H. (2016). Density and seismic velocity of hydrous melts under crustal and upper mantle conditions. *Geochemistry, Geophysics, Geosystems*, *17*, 1799–1814. https://doi.org/10.1002/2015GC006242

Vidale, J. E., Schmidt, D. A., Malone, S. D., Hotovec-Ellis, A. J., Moran, S. C., Creager, K. C., & Houston, H. (2014). Deep long-period earthquakes west of the volcanic arc in Oregon: Evidence of serpentine dehydration in the fore-arc mantle wedge. *Geophysical Research Letters*, *41*, 370–376. https://doi.org/10.1002/2013GL059118

Walker, K. T., Bokelmann, G. H. R., Klemperer, S. L., Bock, G., & The Eifel Team (2007). Seismic anisotropy in the asthenosphere beneath the Eifel. In J. R. R. Ritter, & U. R. Christensen (Eds.), *Mantle Plumes—A Multidisciplinary Approach* (pp. 439–464). Heidelberg: Springer Verlag.

Wech, A. G., Thelen, W. A., & Thomas, A. M. (2020). Deep long-period earthquakes generated by second boiling beneath Mauna Kea volcano. *Science*, *368*(6492), 775–779. https://doi.org/10.1126/science.aba4798

Wilson, M., & Downes, H. (2006). Tertiary-Quaternary intra-plate volcanism in Europe and its relationship to mantle dynamics. In D. G. Gee, & R. A. Stephenspn (Eds.), *European Lithosphere Dynamics* (Vol. 32, pp. 147–166). London, Memours: Geological Society. 0435–4,052/06

Witt-Eickschen, G. (2007). Thermal and geochemical evolution of the shallow subcontinental lithospheric mantle beneath the Eifel: Constraints from mantle xenoliths, a review. In J. R. R. Ritter, & U. R. Christensen (Eds.), *Mantle Plumes, A Multidisciplinary Approach* (pp. 323–367). Heidelberg: Springer.

Wörner, G., & Schmincke, H.-U. (1984). Petrogenesis of the Laacher See tephra sequence (East Eifel, Germany). *Journal of Petrology*, *25*(4), 836–851. https://doi.org/10.1093/petrology/25.4.836

Wüllner, U., Christensen, U. R., & Jordan, M. (2006). Joint geodynamical and seismic modelling of the Eifel plume. *Geophysical Journal International*, *165*, 357–372. https://doi.org/10.1111/j.1365-246X.2006.02906

Yang, J., & Faccenda, M. (2020). Intraplate volcanism originating from upwelling hydrous mantle transition zone. *Nature*, *579*(7797), 88–91. https://doi.org/10.1038/s41586-020-2045-y

Zolitschka, B., Negendank, J., & Lottermoser, B. (1995). Sedimentological proof and dating of the Early Holocene volcanic eruption of Ulmener Maar (Vulkaneifel, Germany). *Geologische Rundschau*, *84*(1), 213–219. https://doi.org/10.1007/bf00192252